A reflection on analytical tornado-like vortex flow field models

Gillmeier, Stefanie; Sterling, Mark; Hemida, Hassan; Baker, Christopher

DOI:
10.1016/j.jweia.2017.12.017

Document Version
Peer reviewed version

Citation for published version (Harvard):
Gillmeier, S, Sterling, M, Hemida, H & Baker, C 2018, 'A reflection on analytical tornado-like vortex flow field models', *Journal of Wind Engineering and Industrial Aerodynamics*, vol. 174, pp. 10-27. https://doi.org/10.1016/j.jweia.2017.12.017

A reflection on analytical tornado-like vortex flow field models

S. Gillmeier[1], M. Sterling[2], H. Hemida[3], C.J. Baker[4]

Department of Civil Engineering, School of Engineering, University of Birmingham, Edgbaston, Birmingham, B15 2TT, United Kingdom, [1]stefaniegillmeier-wls@web.de, [2]m.sterling@bham.ac.uk, [3]h.hemida@bham.ac.uk, [4]c.j.baker@bham.ac.uk

Abstract

Given the difficulties associated with undertaking full-scale measurements in tornadoes, recourse is often made to models. In this field, analytical models have, perhaps surprisingly, stood the test of time, with the Rankine, Burgers-Rott and Sullivan models frequently invoked to model the flow field of a tornado. These mathematical models are by their very nature, a simplification of what is a highly complex phenomenon. However, in many cases they have been represented as the 'truth' without the fundamental assumptions governing the model being either explored in detail or even acknowledged. This paper attempts to rectify this by giving detailed information about assumptions and limitations of each vortex model and critically assesses the ability (or otherwise) of the Rankine, Burgers-Rott, Sullivan, and the recently published Baker vortex model to simulate tornado-like flow. Comparisons are made to the flow field of a physically simulated tornado, which by its very nature is also a model, but arguably more realistic.

It was found that the vortex models are able to represent certain flow patterns at certain heights but fail, due to their simplifications, in replicating the entire three-dimensional flow structure obtained experimentally.

Keywords: Laboratory simulated tornado vortex; Analytical vortex models; Rankine vortex; Burgers-Rott vortex; Sullivan vortex; Baker vortex

1. Introduction

Within the Wind Engineering community, increasing attention is being paid to the effects of non-stationary, non-synoptic winds, i.e. tornadoes. The structure of full-scale tornadoes is highly complex, showing a three-dimensional flow field, instabilities, singularities and non-linear effects (e.g. Lewellen, 1993; Davies-Jones et al., 2001; Alexander and Wurman, 2008; Karstens et al., 2010). In order to understand the physical processes present in a tornado flow field, simplified models are needed, which reduce the degree of freedom present in full-scale observations, and therefore allow a detailed and statistically representative evaluation of velocity and pressure fields. In order to provide this type of datasets, the tornado-like flow field was modelled experimentally

and/or numerically by several authors such as Ward, 1972; Church et al., 1979; Lewellen et al., 1997; Haan et al., 2008; Mishra et al., 2008; Natarajan, 2011; Sabareesh et al., 2012; Refan et al., 2014; Gillmeier et al., 2016; Liu and Ishihara, 2016; Nolan et al., 2017 and Tang et al., 2017. An attempt to analytically model the three-dimensional flow in the boundary layer of a tornado-like vortex was made by Kuo (1971) by alternatingly solving the two nonlinear boundary-layer equations for the radial and vertical distribution of velocities. The Bloor and Ingham vortex model (1987) and the Vyas-Majdalani vortex model (Vyas et al., 2003) are exact inviscid solutions to the Euler's equations in a confined conical and cylindrical domain, respectively. Xu and Hangan (2009) analytically modelled an inviscid tornado-like vortex using a free narrow jet solution combined with a modified Rankine vortex. However, it needs to be mentioned here that this combined model is not an exact solution to the Navier-Stokes-Equations. Wood and White (2011) presented a new parametric model of vortex tangential-wind profiles, which is based on the Vatistas model (Vatistas et al., 1991) and is primarily designed to depict realistic-looking tangential wind profiles observed in atmospheric vortices.

Despite this excellent work, the Rankine (Rankine, 1882), Burgers-Rott (Burgers, 1948; Rott, 1958) and Sullivan (Sullivan, 1959) vortex model are still the most commonly used vortex models to replicate tornado-like flow behaviour. An overview of some of the before mentioned vortex models can be found in e.g. Kilty (2005), Batterson et al. (2007) and Kim and Matsui (2017). However, with the increasing interest in the simulation of tornado-like flows, these models have (in some cases and with varying degrees of success) been invoked in order to describe some elements of the flow field. The authors feel that it is worth reflecting on the fundamental assumptions behind these models and bench marking their performance against measured data obtained in controlled conditions. For that reason, this paper gives detailed information about the derivation and simplifications of the Rankine, Burgers-Rott and Sullivan vortex model. In addition to the Rankine, Burgers-Rott and Sullivan vortex models, the recently published vortex model by Baker and Sterling (2017), hereafter called 'Baker vortex model', is also included in the analysis.

Section two of this paper provides detailed information about the derivation and simplifications of the above mentioned vortex models, while section three outlines the experimental methodology used to assess the model suitability. The results of the model benchmarking can be found in section four, with the main conclusions presented in section five.

2. Existing vortex models

2.1 Flow field notation

In what follows, a cylindrical coordinate system has been adopted as illustrated in figure 1. In figure 1, r, z and θ are the radial distance, vertical distance and circumferential angle, respectively.

Thus, u_r , u_z and u_θ represent the radial, vertical and circumferential components of velocity. For the sake of simplicity the flow is considered to be incompressible for all models and a density of air of ρ = 1.21kg/m^3 is assumed for all calculations. In this section, a brief description of the different vortex models examined in this paper is provided, together with the underlying assumptions.

Using the aforementioned notation, the continuity equation (Eq. *1*) and radial (Eq. *2*), circumferential (Eq. *3*) and vertical (Eq. *4*) components of the Navier-Stokes-Equations (NSE) can be expressed as:

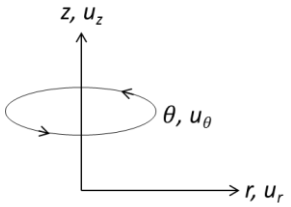

Figure 1: Flow field notation.

$$\underbrace{\frac{1}{r}\frac{\partial(ru_r)}{\partial r}}_{1}+\underbrace{\frac{1}{r}\frac{\partial u_\theta}{\partial \theta}}_{2}+\underbrace{\frac{\partial u_z}{\partial z}}_{3}=0 \qquad (1)$$

$$\underbrace{\frac{\partial u_r}{\partial t}}_{R1}+\underbrace{u_r\frac{\partial u_r}{\partial r}}_{R2}+\underbrace{\frac{u_\theta}{r}\frac{\partial u_r}{\partial \theta}}_{R3}-\underbrace{\frac{u_\theta^2}{r}}_{R4}+\underbrace{u_z\frac{\partial u_r}{\partial z}}_{R5}=$$

$$-\underbrace{\frac{1}{\rho}\frac{\partial p}{\partial r}}_{R6}+\underbrace{g_r}_{R7}+\nu\left(\underbrace{\frac{1}{r}\frac{\partial}{\partial r}\left(r\frac{\partial u_r}{\partial r}\right)}_{R8}-\underbrace{\frac{u_r}{r^2}}_{R9}+\underbrace{\frac{1}{r^2}\frac{\partial^2 u_r}{\partial \theta^2}}_{R10}-\underbrace{\frac{2}{r^2}\frac{\partial u_\theta}{\partial \theta}}_{R11}+\underbrace{\frac{\partial^2 u_r}{\partial z^2}}_{R12}\right) \qquad (2)$$

$$\underbrace{\frac{\partial u_\theta}{\partial t}}_{C1}+\underbrace{u_r\frac{\partial u_\theta}{\partial r}}_{C2}+\underbrace{\frac{u_\theta}{r}\frac{\partial u_\theta}{\partial \theta}}_{C3}+\underbrace{\frac{u_r u_\theta}{r}}_{C4}+\underbrace{u_z\frac{\partial u_\theta}{\partial z}}_{C5}=$$

$$-\underbrace{\frac{1}{\rho r}\frac{\partial p}{\partial \theta}}_{C6}+\underbrace{g_\theta}_{C7}+\nu\left(\underbrace{\frac{1}{r}\frac{\partial}{\partial r}\left(r\frac{\partial u_\theta}{\partial r}\right)}_{C8}-\underbrace{\frac{u_\theta}{r^2}}_{C9}+\underbrace{\frac{1}{r^2}\frac{\partial^2 u_\theta}{\partial \theta^2}}_{C10}-\underbrace{\frac{2}{r^2}\frac{\partial u_r}{\partial \theta}}_{C11}+\underbrace{\frac{\partial^2 u_\theta}{\partial z^2}}_{C12}\right) \qquad (3)$$

$$\underbrace{\frac{\partial u_z}{\partial t}}_{Z1}+\underbrace{u_r\frac{\partial u_z}{\partial r}}_{Z2}+\underbrace{\frac{u_\theta}{r}\frac{\partial u_z}{\partial \theta}}_{Z3}+\underbrace{u_z\frac{\partial u_z}{\partial z}}_{Z4}=$$

$$-\underbrace{\frac{1}{\rho}\frac{\partial p}{\partial z}}_{Z5}+\underbrace{g_z}_{Z6}+\nu\left(\underbrace{\frac{1}{r}\frac{\partial}{\partial r}\left(r\frac{\partial u_z}{\partial r}\right)}_{Z7}+\underbrace{\frac{1}{r^2}\frac{\partial^2 u_z}{\partial \theta^2}}_{Z8}+\underbrace{\frac{\partial^2 u_z}{\partial z^2}}_{Z9}\right) \qquad (4)$$

Here ρ is the density of the fluid, t is the time, p is the static pressure and $\vec{g}$ is the gravity vector in its different components. The different terms in equations (*1 – 4*) have been labelled since, as will be demonstrated below, it is possible to derive the majority of the analytical models by disregarding different terms.

2.2 Rankine vortex model

The Rankine model has been adopted by a number of researchers (e.g. Hoecker, 1960; Church et al., 1979; Winn et al., 1999; Wurman and Gill, 2000; Brown and Wood, 2004; Lee et al., 2004; Mishra et al., 2008; Bech et al., 2009; Hashemi Tari et al., 2010; Wood and Brown, 2011; Refan and Hangan, 2016; Tang et al., 2017) to model tornado-like flow behaviour. The following assumptions are made in the derivation of the Rankine vortex model:

- *The flow field is one-dimensional and as such equations (2) and (4) can be disregarded.*
- *The flow field is steady state, i.e., term R1 can be taken as zero.*
- *The flow is inviscid (μ=0), i.e., terms R8 - R12 can be neglected.*
- *Body forces can be neglected, i.e., ($\vec{g}$=0).*

These assumptions reduce the NSE to the cyclostrophic equation (Eq. *5*).

$$\frac{dp(r)}{dr} = \rho \frac{u_\theta(r)^2}{r} \tag{5}$$

The Rankine model also assumes that the flow consists of two separate flow regions. In the first region, the core region (i.e., $r < R$, where R is the core radius, which is defined as the radial distance from the vortex centre at which the circumferential velocity component is maximal), the flow is assumed to have a constant vorticity and is considered to be similar to that of a solid body. In the second region, ($r > R$) it is assumed that the flow can be described by a potential flow field (incompressible, inviscid and irrotational) (Alekseenko et al., 2007) and is inversely proportional to the radial distance. These assumptions enable the circumferential velocity component to be modelled via an expression of the form:

$$\overline{u_\theta}(\bar{r}) = \begin{cases} \bar{r} & for\ (\bar{r} < 1) \\ \frac{1}{\bar{r}} & for\ (\bar{r} > 1) \end{cases} \tag{6}$$

where $\overline{u_\theta}$ is the normalised circumferential velocity component ($= u_\theta / u_{\theta,max}$, where $u_{\theta,max}$ is the maximum value of u_θ) and $\bar{r}$ is the radial distance normalised by the core radius, R. In equation *6*, a discontinuity occurs at $\bar{r} = 1$. In order to avoid this, the model is occasionally modified as shown in equation *6.1*. However, the most commonly used form is shown in equation *6* and hence will be used in what follows.

$$\overline{u_\theta}(\bar{r}) = \frac{2\bar{r}}{(1+\bar{r}^2)} \qquad (6.1)$$

Combining equation (*6*) with equation (*5*) and integrating, yields an expression for the normalised pressure distribution of the Rankine vortex model (Eq. *7*):

$$\bar{p}(\bar{r}) = \begin{cases} \overline{p_{(r=0)}} + \frac{1}{2}\left(\frac{r}{R}\right)^2 & for\ (\bar{r} < 1) \\ \overline{p_{r\to\infty}} - \frac{1}{2}\left(\frac{R}{r}\right)^2 & for\ (\bar{r} > 1) \end{cases} \qquad (7)$$

where $\bar{p}(\bar{r})$ is the normalised pressure ($= p(r)/\ \rho {u_{\theta,max}}^2$), $\overline{p_{r\to\infty}}$ is the normalised static pressure, which is unaffected by the vortex and $\overline{p_{(r=0)}}$ is the static pressure at the vortex centre.

2.3 Burgers-Rott vortex model

The Burgers-Rott model has been adopted by a number of authors (e.g. Winn et al., 1999; Brown and Wood, 2004; Lee et al., 2004, Kosiba and Wurman, 2010; Wood and Brown, 2011; Wurman et al., 2013) to model tornado-like flow behaviour. Explicit in the derivation of the model are the following assumptions:

- *The flow field is steady state, i.e., terms R1, C1 and Z1 are taken as zero.*
- *The viscosity is considered to be constant throughout the entire flow field.*
- *Body forces can be neglected, i.e., ($\vec{g}$=0).*
- *The circumferential velocity component is assumed to be solely dependent on the radial distance ($u_\theta = u_\theta(r)$).*
- *The vertical velocity component is assumed to be solely and linearly dependent on the vertical distance ($u_z = u_z(z)$ and $u_z \propto z$).*
- *As a result of the last two assumptions, the radial velocity component is solely and linearly dependent on the radial distance ($u_r = u_r(r)$ and $u_r \propto r$).*
- *The static pressure is assumed to be solely dependent on radial and vertical distances ($p = p(r,z)$).*

The above assumptions reduce equations (*1 – 4*) to the following simplified versions:

$$\frac{1}{r}\frac{\partial(ru_r)}{\partial r} + \frac{\partial u_z}{\partial z} = 0 \qquad (1^*)$$

$$u_r\frac{\partial u_r}{\partial r} - \frac{u_\theta^2}{r} = -\frac{1}{\rho}\frac{\partial p}{\partial r} + \nu\left(\frac{1}{r}\frac{\partial}{\partial r}\left(r\frac{\partial u_r}{\partial r}\right) - \frac{u_r}{r^2}\right) \qquad (2^*)$$

$$u_r \frac{\partial u_\theta}{\partial r} + \frac{u_r u_\theta}{r} = \nu \left(\frac{1}{r} \frac{\partial}{\partial r} \left(r \frac{\partial u_\theta}{\partial r} \right) - \frac{u_\theta}{r^2} \right) \quad (3^*)$$

$$u_z \frac{\partial u_z}{\partial z} = -\frac{1}{\rho} \frac{\partial p}{\partial z} \quad (4^*)$$

Now, the Burgers-Rott model acknowledges that the flow within a tornado-like structure is likely to be subject to changing levels of vorticity, which in turn will have implications for the associated pressure field. Thus, it is assumed that the vertical velocity component changes with respect to height and the following relationship is adopted:

$$\overline{u_z}(\bar{z}) = 2\bar{a}\bar{z} \quad (8)$$

where $\overline{u_z}(\bar{z})$ is the normalised vertical velocity ($= u_z(z)/u_{\theta,max}$), $\bar{z}$ is the normalised vertical height ($= z/R$) and $\bar{a}$ is a constant, whose magnitude purports to account for the strength of vortex stretching. It is also assumed that $\bar{a}$ is related to the viscous dissipation, ν, via an expression of the form:

$$\bar{a} = \frac{2\nu}{R u_{\theta,max}} \quad (8.1)$$

Equation (*8.1*) implies that the viscous dissipation, ν, continuously removes kinetic energy from the flow, which is continuously introduced by vortex stretching. Using equation (*8*) and integrating the simplified continuity equation (Eq. *1**), an expression for the normalised radial velocity component, $\overline{u_r}$, can be obtained (Eq. *9*).

$$\overline{u_r}(\bar{r}) = -\bar{a}\bar{r} \quad (9)$$

Using equations (*8*) and (*9*), and solving the simplified NSE in the circumferential direction (Eq. *3**), an expression for the normalised circumferential velocity component, $\overline{u_\theta}$, can be found (Eq. *10*).

$$\overline{u_\theta}(\bar{r}) = \frac{1}{\bar{r}} \left(1 - exp(-\bar{r}^2) \right) \quad (10)$$

It is perhaps worth noting that $\overline{u_z}$ and $\overline{u_r}$ increase to infinity as $\bar{z} \to \infty$ and $\bar{r} \to \infty$, respectively, which, it is suggested, may not be representative of a tornado-like flow structure.

The pressure distribution of the Burgers-Rott vortex model can be obtained by solving the simplified NSE (Eq. *2** and Eq. *4**) using the model velocities (Eq. *8*, Eq. *9*, and Eq. *10*). This leads to the following equation for the normalised pressure distribution (Eq. *11*).

$$\overline{p_{Burgers}}(\bar{r}, \bar{z}) = \bar{p}(0,0) + \int_0^{\bar{r}} \frac{\overline{u_\theta}(\bar{r}')^2}{\bar{r}'} d\bar{r}' - \frac{\bar{a}^2}{2} (\bar{r}^2 + 4\bar{z}^2) \quad (11)$$

2.4 Sullivan vortex model

The Sullivan model has also been adopted by a few researchers (e.g. Winn et al., 1999; Wood and Brown, 2011) to model tornado-like flow behaviour. The assumptions for this vortex model are:

- *The flow field is steady state, i.e., terms R1, C1 and Z1 are taken as zero.*
- *The viscosity is considered to be constant throughout the entire flow field.*
- *Body forces can be neglected, i.e., ($\vec{g}$=0).*
- *The circumferential velocity component is assumed to be solely dependent on the radial distance ($u_\theta = u_\theta(r)$).*
- *The vertical velocity component is assumed to be only dependent on radial and vertical distances. The dependence on the vertical distance is linear ($u_z = u_z(r,z)$ and $u_z \propto z$).*
- *As a result of the last two assumptions, the radial velocity component is solely dependent on the radial distance ($u_r = u_r(r)$).*
- *The static pressure is assumed to be solely dependent on radial and vertical distances ($p = p(r,z)$).*

The above assumptions reduce the continuity equation (*1*), radial and circumferential components of the NSE (*2 – 3*) to simplified versions shown in equations (*1* – 3**). For the vertical component of the NSE (*4*) the following simplified versions is obtained.

$$u_z \frac{\partial u_z}{\partial z} + u_z \frac{\partial u_z}{\partial z} = -\frac{1}{\rho}\frac{\partial p}{\partial z} + \nu\left(\frac{1}{r}\frac{\partial}{\partial r}\left(r\frac{\partial u_z}{\partial r}\right)\right) \qquad (4^{**})$$

One main difference of the Sullivan model compared to the Burgers-Rott model lies in the complexity of the model solution. While the Burgers-Rott vortex model only allows single-celled vortices to be generated, the Sullivan model potentially enables solutions for single and two-celled vortices to be obtained; this is obtained via the use of a shape parameter, *b* (Eq. *12* and Eq. *13*). The effect of this parameter on the tornado-like flow field will be discussed in detail in section 2.7. Unless stated otherwise, *b* = 3. The required vortex stretching is generated by suction at relatively large heights and is achieved by a non-linear increase of the vertical velocity component with height, as illustrated in equation (*12*). The same normalisation used for the Burgers-Rott vortex model is applied for the Sullivan vortex model.

$$\overline{u_z}(\bar{r},\bar{z}) = 2\bar{a}\bar{z}\left(1 - b\cdot exp(-\bar{r}^2)\right) \qquad (12)$$

Following the procedure described for the Burgers-Rott vortex model, expressions for $\overline{u_r}$ (Eq. *13*) and $\overline{u_\theta}$ (Eq. *14*) can be obtained.

$$\overline{u_r}(\bar{r}) = -\bar{a}\bar{r} + \frac{2b\bar{v}}{\bar{r}}\left(1 - exp(-\bar{r}^2)\right) \quad (13)$$

$$\overline{u_\theta}(\bar{r}) = \frac{1}{\bar{r}}\frac{H(x)}{H(\infty)} \quad (14)$$

$$with\ x = \bar{r}^2 \quad and\ H(x) = \int_0^x exp\left(-x' + 3\int_0^{x'}\frac{1}{x''}\left(1 - exp(-x'')\right)dx''\right)dx'$$

It is perhaps worth noting, that for $\bar{r}$ = 0 and $\bar{z} \to \infty$ the magnitude of $\overline{u_z}$ increases to infinity. Furthermore, also $\overline{u_r}$ increases to infinity for $\bar{r} \to \infty$ (Eq. *13*). Similar to the Burgers-Rott model, it is suggested that this behaviour may be physically unrealistic in a tornado-like structure.

The pressure distribution of the Sullivan vortex model can be obtained by solving the simplified NSE (Eq. *2** and *4**) using the model velocities (Eq. *12 - 14*). This leads to the following equation for the normalised pressure distribution:

$$\overline{p_{Sullivan}}(\bar{r}, \bar{z}) = \overline{p_{Burgers}}(\bar{r}, \bar{z}) - \frac{18\bar{v}^2}{\bar{r}^2}\left(1 - exp(-\bar{r}^2)\right)^2 \quad (15)$$

2.5 Baker vortex model

Baker and Sterling (2017) developed a vortex model, which can reproduce the flow and pressure characteristics of a single and two-celled vortex. In order to enable comparisons with the aforementioned models, only the solution for the single-cell vortex with radial inflow and vertical updraft is analysed in this paper. The following assumptions are made in the derivation of the Baker vortex model:

- *The flow field is steady state, i.e., terms R1, C1 and Z1 are taken as zero.*
- *The flow is inviscid, i.e., terms R8 - R12, C8 - C12 and Z7 - Z9 can be disregarded.*
- *Body forces can be neglected, i.e., ($\vec{g}$=0).*
- *The circumferential velocity component is assumed to be dependent on radial and vertical distance* ($u_\theta = u_\theta(r, z)$).
- *The radial velocity component is assumed to be only dependent on radial and vertical distances* ($u_r = u_r(r, z)$).
- *As a result of the last two assumptions, the vertical velocity component is solely dependent on radial and vertical distances ($u_r = u_r(r, z)$).*
- *The static pressure is assumed to be solely dependent on radial and vertical distances ($p = p(r, z)$).*

These assumptions reduce the continuity equation (*1*) to the simplified version shown in equation (*1**) and the NSE (Eq. *2 - 4*) to the following simplified versions:

$$u_r \frac{\partial u_r}{\partial r} - \frac{u_\theta^2}{r} + u_z \frac{\partial u_r}{\partial z} = -\frac{1}{\rho}\frac{\partial p}{\partial r} \quad (2^{***})$$

$$u_r \frac{\partial u_\theta}{\partial r} + \frac{u_r u_\theta}{r} + u_z \frac{\partial u_\theta}{\partial z} = 0 \quad (3^{***})$$

$$u_r \frac{\partial u_z}{\partial r} + u_z \frac{\partial u_z}{\partial z} = -\frac{1}{\rho}\frac{\partial p}{\partial z} \quad (4^{***})$$

In addition, the Baker model assumes that the radial velocity component takes the following form:

$$\overline{u_r}(\bar{r}, \bar{z}) = \frac{-4\bar{r}\bar{z}}{(1+\bar{r}^2)(1+\bar{z}^2)} \quad (16)$$

One of the potential advantages of this model compared to the Rankine, Burgers-Rott and Sullivan vortex models is that the radial velocity component is assumed to show a more realistic behaviour (Eq. *16*), i.e., rather than increasing to infinity for large radial distances, a maximum value is reached at $r = r_m$ which then falls to zero for $r = 0$ and $r = \infty$. In the vertical direction, the radial velocity distribution shows an attempt to replicate the tornado boundary layer by assuming a maximum in the radial velocity component at a known distance above the ground ($z = z_m$). For $z = 0$ and $z = \infty$ the radial velocity falls to zero. Since the Baker vortex model focuses on the distribution of the radial velocity component, different parameters are chosen for the normalisation of velocities, radial and vertical distances. Velocities are normalised by the maximum radial velocity ($u_r(r_m, z_m) = u_{r,max}$) and radial and vertical distances are normalised by r_m and z_m, respectively.

Using equation (*16*) and integrating the simplified continuity equation (*1**), an expression for the normalised vertical velocity component, $\overline{u_z}$, can be obtained as follows:

$$\overline{u_z}(\bar{r}, \bar{z}) = \frac{4\delta\, ln(1+\bar{z}^2)}{(1+\bar{r}^2)^2} \quad (17)$$

where δ is the ratio z_m / r_m. Using equations (*16*) and (*17*), and solving the simplified NSE in the circumferential direction (Eq. *3****), the following expression for the normalised circumferential velocity component, $\overline{u_\theta}$, can be obtained:

$$\overline{u_\theta}(\bar{r}, \bar{z}) = \frac{K\bar{r}^{\gamma-1}\left[ln(1+\bar{z}^2)\right]^{\gamma/2}}{(1+\bar{r}^2)^{\gamma/2}} \quad (18)$$

Here, γ is a shape parameter (an arbitrary real number which can be used to adjust the shape of the circumferential velocity profile). *K* is a constant and related to Baker's definition of the swirl ratio, i.e., $S_{Baker} = 0.347\,K$. The swirl ratio in the Baker vortex model is defined as the ratio of $u_\theta(r_m, z_m)$ and $u_r(r_m, z_m)$. It is perhaps worth noting that $\overline{u_\theta}$ increases to infinity for $z \to \infty$. This increase is

assumed to be realistic for the lowest heights, relatively close to the surface, where surface roughness affects the vertical velocity distribution but becomes physically unrealistic for larger heights.

The pressure distribution of the Baker vortex model can be obtained by solving the simplified NSE (Eq. *2**** and Eq. *4****) using the model velocities (Eq. *16 – 18*) and, assuming a shape parameter of $\gamma = 2$:

$$\overline{p_{Baker}}(\bar{r},\bar{z}) = -\frac{8\bar{r}^2\bar{z}}{(1+\bar{r}^2)^2(1+\bar{z}^2)^2} - \frac{4.15{S_{Baker}}^2\left(ln(1+\bar{z}^2)\right)^2}{(1+\bar{r}^2)} - \frac{4ln(1+\bar{z}^2)(1-\bar{z}^2)}{(1+\bar{r}^2)^2(1+\bar{z}^2)^2} \qquad (19)$$

It is worth noting that the surface pressure distribution equals zero for $z = 0$. This behaviour is physically unrealistic in a tornado-like structure and is discussed in Baker and Sterling (2017). It is assumed that pressure variations in the vertical direction can be neglected within the boundary layer ($z < z_m$) (Baker and Sterling, 2017) and consequently, it is assumed that $\overline{p_{Baker}}(\bar{r},\bar{z}<1) = \overline{p_{Baker}}(\bar{r},\bar{z}=1)$.

2.6 Circumferential velocity component

Unlike the Rankine, Burgers-Rott and Sullivan vortex models, the Baker model has a shape parameter, γ, which enables the shape of the circumferential velocity profile to be varied. The effect of this parameter on the circumferential velocity field is illustrated in table 1 and figure 2. It is perhaps worth noting that γ is related to $\bar{r}$ in the following way ($\bar{r}^2 = \gamma - 1$) (Baker and Sterling, 2017). Consequently, for $\gamma \leq 1$, the circumferential velocity component becomes physically unreasonable. Thus, to ensure results, which describe the behaviour of a forced vortex at the centre, and a free vortex at larger radial distances, Baker and Sterling (2017) recommend setting $\gamma = 2$.

Table 1 illustrates the ratio of $u_{\theta,max}$ and *R* of the corresponding models compared to the Rankine vortex model with input parameters of *R* = 10m and $u_{\theta,max}$ = 10m/s. For the Baker vortex model a swirl ratio of $S_{Baker} = 1$ is assumed and readings for the maximum circumferential velocity component are taken at $z = z_m$. Table 1 shows that Burgers-Rott and Sullivan vortex models underestimate the actual input velocity by a factor of *0.64* and *0.32*, respectively, and overestimate the core radius position, *R*, by a factor of *1.12* and *2.29* respectively. For the Baker vortex model with a shape parameter of $\gamma = 2$, the radius at which $\overline{u_r}$ attains a maximum, is identical to the core radius of the Baker vortex model and is also identical to the actual input core radius ($r_m = R_{Baker} = R$). Hence, the Rankine and Baker model results for $\gamma = 2$ in table 1 are identical. With increasing γ, R_{Baker} increases and the magnitude of $u_{\theta,max,Baker}$decreases (Table 1). For $\gamma = 3$, *R* and $u_{\theta,max}$ of Baker and Burgers-Rott vortex model are similar and show a decrease in $u_{\theta,max}$ by about $1/3 \times u_{\theta,max,Rankine}$(Table 1). For $\gamma = 5$, *R* and $u_{\theta,max}$ of Baker and Sullivan vortex model are

similar and show a core radius, which is about $2 \times R_{Rankine}$ and a decrease in $u_{\theta,max}$ by about $2/3 \times u_{\theta,max,Rankine}$ (Table 1). Thus, in what follows, care has been taken to normalise, by the relevant model values of each vortex model as opposed to a standard value.

Table 1: Ratios of $u_{\theta,max}$ and R of the corresponding vortex models compared to the Rankine vortex model.

	$\frac{u_{\theta,max,x}}{u_{\theta,max,Rankine}}$	$\frac{R_x}{R_{Rankine}}$
x=Rankine	*1*	*1*
x=Burgers	*0.64*	*1.12*
x=Sullivan	*0.32*	*2.29*
x=Baker (γ=2, $z=z_m$)	*1*	*1*
x=Baker (γ=3, $z=z_m$)	*0.64*	*1.41*
x=Baker (γ=5, $z=z_m$)	*0.33*	*2.0*

Figure 2 shows that among the four vortex models, large differences in the circumferential velocity are found for $r < R_{model}$ between Sullivan and Baker vortex model with a shape parameter of $\gamma = 2$ (Figure 2). This is not surprising as these vortex models represent two entirely different tornado flow types. The Sullivan model represents a two-celled vortex whereas the Baker model shows a single-celled vortex structure. A single-celled vortex is defined as a relatively narrow column of rising and rotating air. With increasing rotational energy, a downdraft forms in the vortex centre and terminates aloft a stagnation point above which the vortex increases significantly in size (Trapp, 2000). This vortex transformation is known as 'vortex breakdown'. With a further increase in rotational energy, the stagnation point lowers towards the ground. In a two-celled vortex, the downdraft reaches the ground and therefore decreases $\overline{u_\theta}$ close to $r = 0$ whereas the structure of the single-celled vortex shows a strong non-linear increase of $\overline{u_\theta}$ inside the vortex core ($r < R_{model}$) (Figure 2).

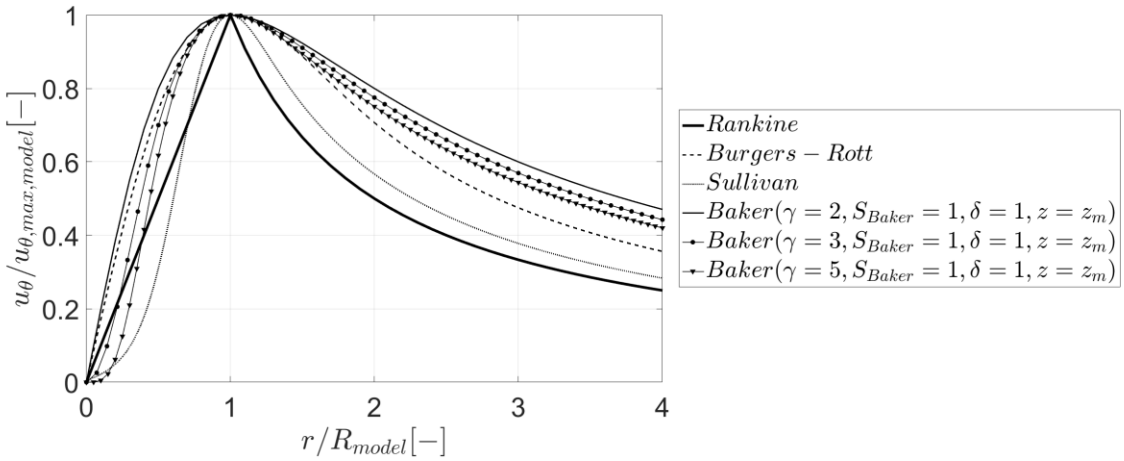

Figure 2: Circumferential velocity component of the Rankine, Burgers-Rott, Sullivan and Baker vortex model.

For the Baker model, close to the vortex core, $\overline{u_\theta}$ increases at a slower rate with increasing γ, and the circumferential velocity profile tends towards the shape of a two-celled vortex structure (Figure 2) (compared to the Sullivan vortex model). For larger radial distances ($r > R_{model}$), $\overline{u_\theta}$ of the Baker vortex model decreases at a slower rate compared to the other three models and largest differences are found between Rankine and Baker vortex model (γ = 2). Differences in the circumferential velocity of all vortex models decrease as $r \to \infty$.

The effect of γ on the circumferential velocity component with height is shown in Figure 3. For relatively small vertical distances from the surface, $\overline{u_\theta}$ increases at a slower rate the larger γ is. With increasing vertical distance, this behaviour reverses and $\overline{u_\theta}$ increases faster with height as γ increases (Figure 3). Furthermore, figure 3 shows that independent from γ, $\overline{u_\theta}$ increases to infinity for $z \to \infty$, albeit at different rates. It needs to be mentioned that the Baker vortex model is the only model that takes a height dependence of u_θ into account. However, it does not represent the vertical profile of the circumferential velocity observed in simulated tornado-like vortices or full-scale. For instance, Tang et al. (2017) showed that u_θ increases rapidly in the lowest heights with the maximum circumferential velocity relatively close to the ground. With further increasing height $\overline{u_\theta}$ decreases and remains relatively uniform in even greater heights. Refan et al. (2017) showed that a similar behaviour was observed in five different full-scale tornadoes of different intensity and flow structure.

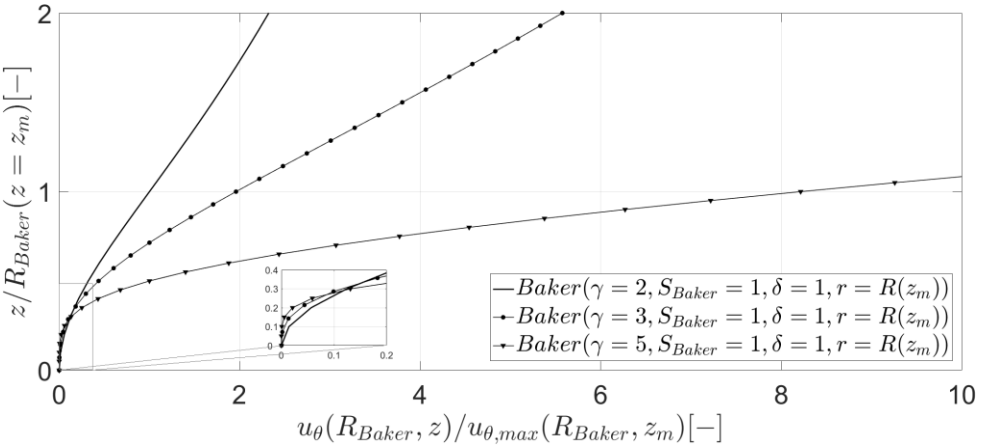

Figure 3: Circumferential velocity component of the Baker vortex model in different heights for different γ values.

Another parameter that influences the shape of the circumferential velocity profile is the swirl ratio, S_{Baker}. The magnitude of u_θ increases as the value of S_{Baker} increases. The position of the core radius and the shape of the circumferential velocity profile are independent from the chosen swirl ratio. For that reason, the effect of S_{Baker} on u_θ cannot be seen when normalising u_θ with $u_{\theta,max,Baker}$ and radial distances with R_{Baker}.

2.7 Radial and vertical velocities and shape parameters

The Baker model is not the only model to employ a shape component. As shown in equation (*8*) and (*12*), both, the Burgers-Rott and Sullivan model also include a 'constant' to 'correct' the vertical velocity. In addition, both models have a 'viscosity' parameter explicitly included in the circumferential velocity component (which is not evident in equations (*10*) and (*14*) due to the normalisation adopted and assuming the relationship given in equation (*8.1*)). If it is assumed that the viscosity parameter corresponds to the kinematic viscosity of air (i.e., $\nu \sim 10^{-5}$ m^2s^{-1} at 20 °C), then the calculated radial and vertical velocity components of the Burgers-Rott and Sullivan vortex models are small. Hence, to ensure reasonable magnitudes of the velocity components (Figures 4 and 5), the viscosity needs to be increased by several orders of magnitude (Davies-Jones and Kessler, 1974). Thus, in this context, the 'viscosity' parameter is essentially nothing more than a 'simple' shape parameter.

Figures 4 and 5 show the effect of the 'viscosity' parameter on the radial and vertical velocity distributions of the Burgers-Rott and Sullivan vortex models. For the Burgers-Rott vortex model, a larger 'viscosity' parameter results in larger vertical and radial velocities (Figure 4). Hence, the larger the value of ν becomes, the greater the radial inflow towards the vortex centre and the stronger the vertical updraft gets (Figure 4). For the Sullivan vortex model, an increase in ν results in larger negative vertical velocities for $r < R_{Sullivan}$, and larger positive vertical velocities for $r > R_{Sullivan}$ (Figure 5). For the radial velocity, the larger ν is, the stronger the radial outflow at $r <$

$R_{Sullivan}$, and the stronger the radial inflow for $r < R_{Sullivan}$ gets (Figure 5). The radial distance at which radial and vertical velocity components change sign is not affected by changes in the 'viscosity' parameter (Figure 5). This means that the size of the downdraft region close to $r = 0$ is independent of ν.

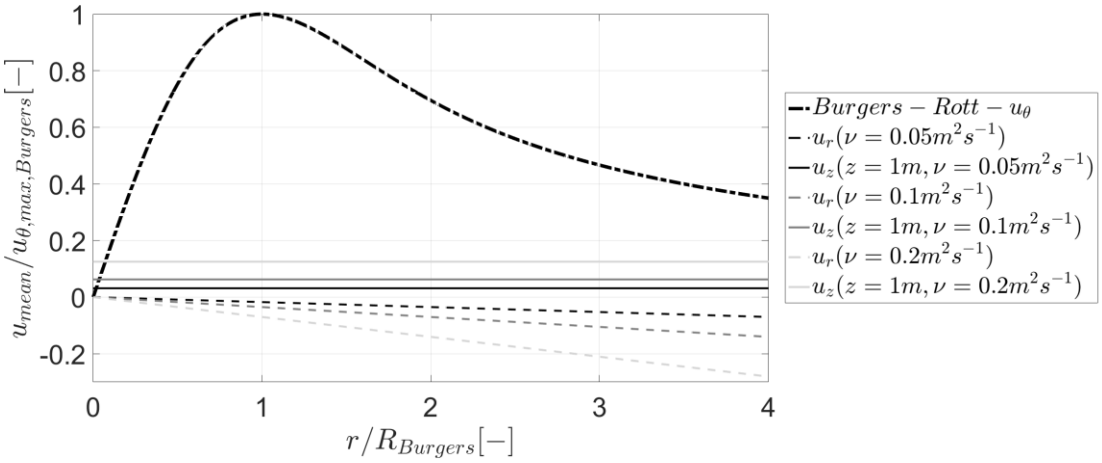

Figure 4: Velocity components of the Burgers-Rott vortex model for different 'viscosity' values.

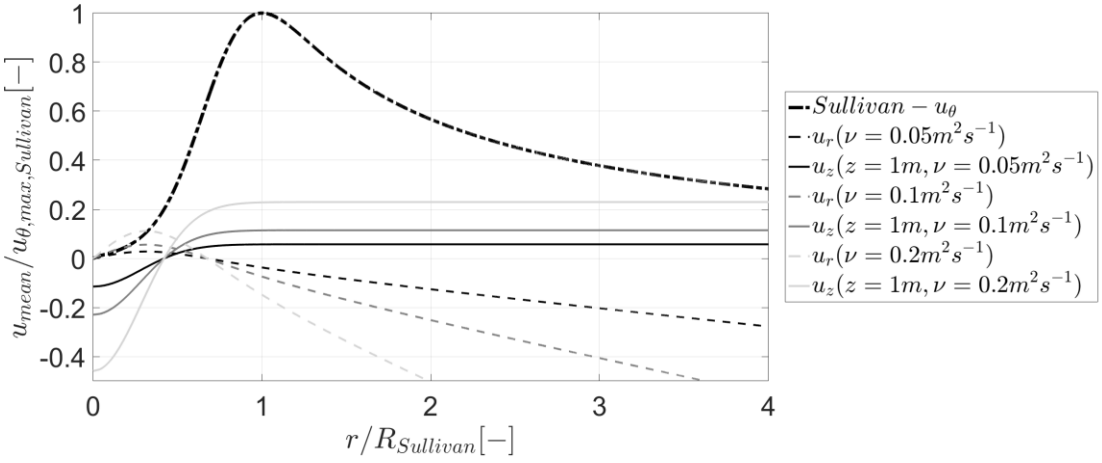

Figure 5: Velocity components of the Sullivan vortex model for different 'viscosity' values.

An additional shape parameter contained in the Sullivan vortex model is denoted as b, which influences the distribution of radial and vertical velocity components and can be adjusted to model solutions for single and two-celled vortices. Figure 6 illustrates the effect of b on the radial and vertical flow field of the Sullivan vortex model. For $b = 0$, radial and vertical velocity components of the Sullivan vortex model are identical to the solutions obtained from the Burgers-Rott vortex model. For $b > 1$, a two-celled structure can be obtained, which is indicated by negative vertical velocities close to the vortex centre. The greater the magnitude of b gets, the more negative the vertical velocities in the vortex centre become, and additionally, the further the downdraft region extends in the radial direction. For $r > R_{Sullivan}$, the vertical velocity converges to a value, which is independent of b but dependent on the height. Radial outflow velocities inside the vortex core are

larger for larger *b* values, and the larger *b* gets, the larger the region of radial outflow extends radially (Figure 6). Radial inflow velocities obtained with a lower *b* value increase slightly faster in magnitude close to the vortex core but converge for larger radial distances (Figure 6). Hence, differences of *b* are only significant inside the vortex core.

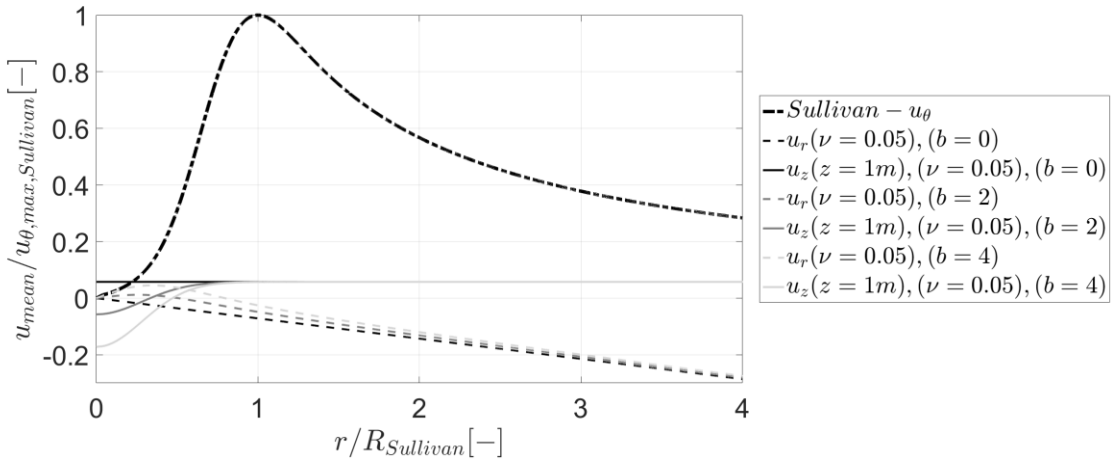

Figure 6: Velocity components of the Sullivan model for different *b* values.

The vertical velocity component of the Baker vortex model depends on the value of δ. The vertical velocity component at the vortex centre increases with increasing δ (Figure 7a). Additionally, figure 7b shows that the vertical velocity component increases faster with height as δ increases.

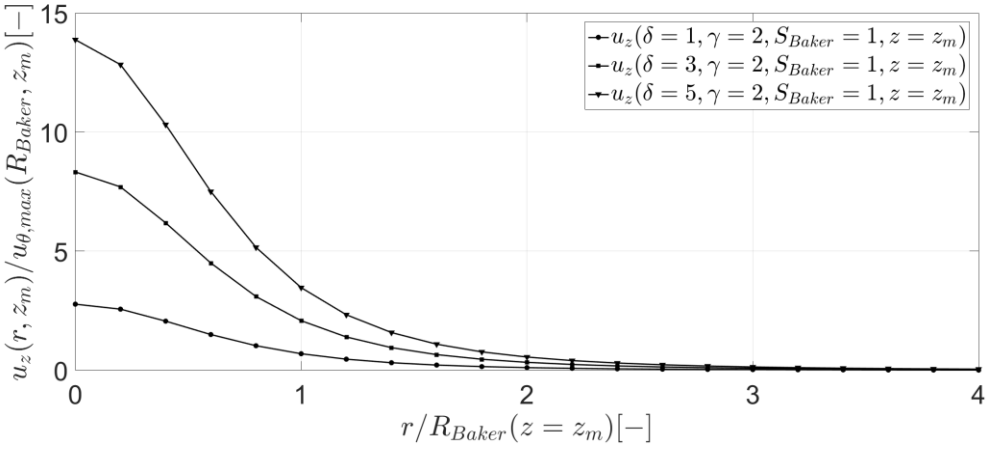

a)

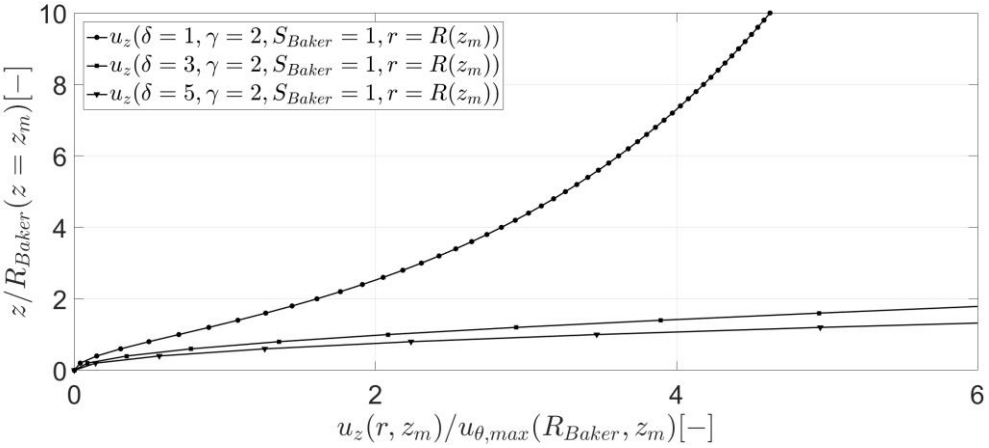

b)

Figure 7: The effect of δ on the vertical velocity component of the Baker vortex model for different radial distances (a) and heights (b).

2.8 The static surface pressure distribution

The surface pressure distribution of Rankine, Burgers-Rott and Sullivan vortex models are shown in figure 8 for the case of $v = 0$. This restriction implies that the surface pressure distributions of the Burgers-Rott and Sullivan vortex models are solely dependent on the circumferential velocity profile of the corresponding vortex model and equations (*11*) and (*15*) simplify to:

$$\overline{p_{Burgers}}(\bar{r}, \bar{z}) = \overline{p_{Sullivan}}(\bar{r}, \bar{z}) = \bar{p}(0,0) + \int_0^{\bar{r}} \frac{\overline{u_\theta}(\bar{r}')^2}{\bar{r}'} d\bar{r}'. \qquad (20)$$

The last term on the right hand side gives the largest contribution to the entire pressure distribution of the Burgers-Rott and Sullivan vortex model. Thus, its value defines the magnitude of surface pressure increase from the vortex centre towards larger radial distances and is determined by the area under the circumferential velocity profile shown in figure 2. For that reason, this term is largest for the Burgers-Rott vortex model and results in what maybe a physically unrealistic surface pressure increase from the vortex centre (Figure 8). For the Sullivan vortex model, the magnitude of this term is of the same order as that one of the Rankine vortex model.

The entire pressure distribution of the Burgers-Rott and Sullivan vortex models, depend on the contribution of the circumferential, radial and vertical velocity (Eq. *11* and Eq. *15*), and therefore is dependent on the 'viscosity' parameter. Also shown in Figure 8, is the effect of *v* on the pressure distribution. The decrease in surface pressure with increasing radial distance originates from a combination of the vertical updraft and the potentially unrealistic increase in radial velocity, i.e., $\frac{\bar{a}^2}{2}(\bar{r}^2 + 4\bar{z}^2)$. These terms are identical in Burgers-Rott and Sullivan vortex models, however, the different trends shown in figure 8 arise due to the normalisation, since $R_{Sullivan} > R_{Burgers\text{-}Rott}$.

The additional term in the surface pressure distribution of the Sullivan vortex model (i.e., $-\frac{18\bar{v}^2}{\bar{r}^2}\left(1-exp(-\bar{r}^2)\right)^2$) describes the effect of the non-linear behaviour of radial and vertical velocity components inside the vortex core on the pressure distribution. The downdraft close to the centre of the vortex increases the surface pressure distribution and places the minimum pressure at the radial position where vertical and radial velocity components are zero (Figure 8).

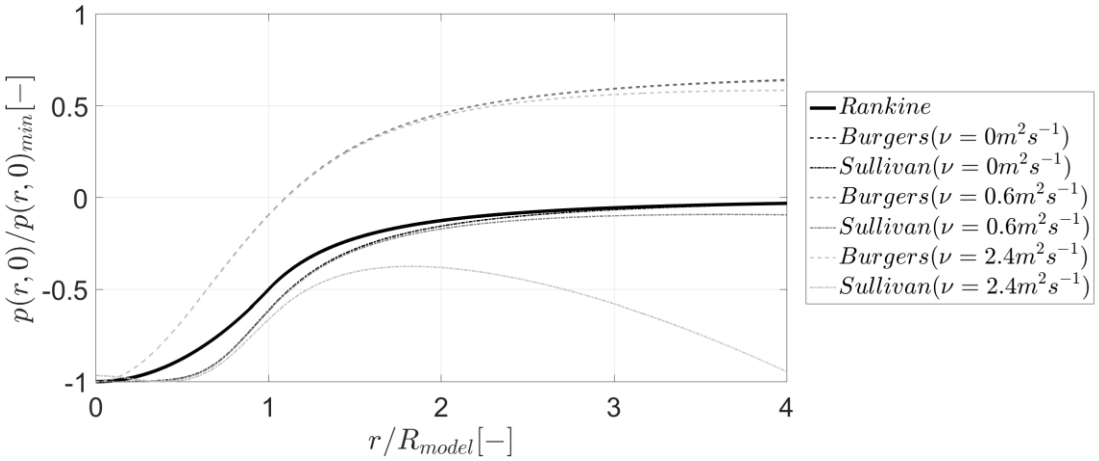

Figure 8: Surface pressure distribution of Rankine, Burgers-Rott and Sullivan vortex model for different 'viscosity' values.

In order to enable a meaningful comparison of the surface pressure distributions, the 'viscosity' parameter, *v*, and the 'vortex stretching' parameters $\overline{a}$, need to be adjusted in the circumferential velocity and surface pressure distribution of the Burgers-Rott vortex model. This ensures that the increase in surface pressure is of similar order to that one of the Rankine and Sullivan vortex model. Thus, equation (*10*) needs to be modified by means of the relation given in equation (*8.1*) in the following way (Eq. *21*) to obtain a circumferential velocity distribution for the Burgers-Rott vortex model, which is dependent on *v* and $\bar{a}$ (Eq. *21*).

$$\overline{u_\theta}(\bar{r}) = \frac{1}{\bar{r}}\left(1-exp\left(-\frac{r\bar{a}\ u_{\theta,max}}{2\nu}\right)^2\right) \qquad (21)$$

v and $\bar{a}$ need to be chosen independent from one another, which has the consequence that the input parameters, *R* and $u_{\theta,max}$ vary (see Eq. *8.1*). Unquestionably, this is physically not consistent but seems to be the only way for the Burgers-Rott vortex model to generate a physically meaningful surface pressure increase with increasing radial distance.

Figure 9 shows the surface pressure distribution for input parameters of *R* = 10m and $u_{\theta,max}$ = 10m/s for the Rankine, Burgers-Rott and Sullivan models. It is worth noting that the 'viscosity' and 'stretching' parameter differ for different input parameters. The two-celled structure of the Sullivan vortex, and hence, the decreased circumferential velocity component close to the vortex core result in a relatively flat pressure distribution close to the vortex centre (Figure 8). The surface

pressure distribution of the Burgers-Rott vortex increases at a faster rate close to the vortex centre due to a rapid increase in circumferential velocity in this region (Figure 8). The largest differences in the surface pressure distribution of the vortex models can be found inside the vortex core ($r < R_{model}$) and for radial distances around $r / R_{model} = 1.5$. This arises due to the relative differences in the magnitude of the circumferential velocity predicted by the analytical models (section 2.6).

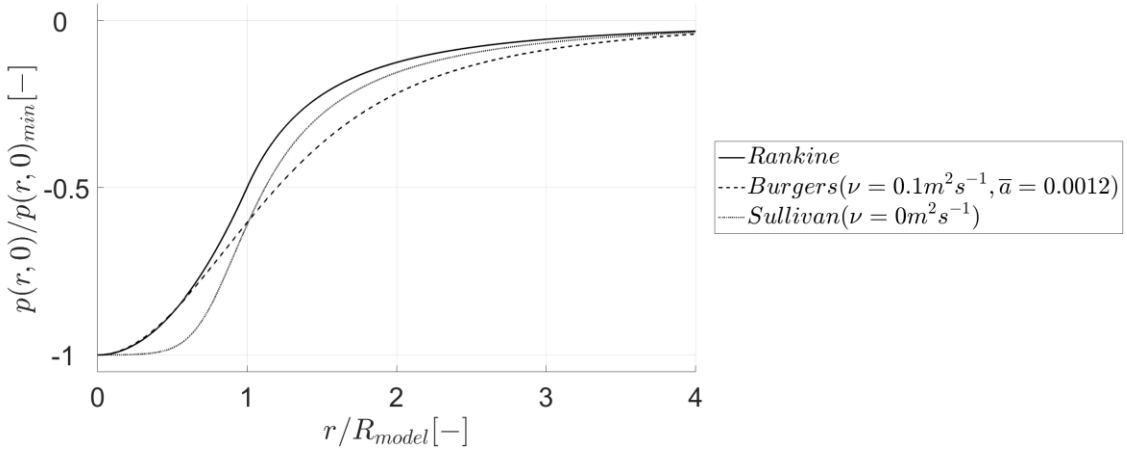

Figure 9: Surface pressure distribution of Rankine, adjusted Burgers-Rott and Sullivan vortex model.

The static 'surface pressure' distribution and the effect of the swirl ratio on the shape of the distribution of the Baker vortex model is shown in figure 10. The 'surface pressure' distribution of the Baker vortex model falls to zero for $r \to \infty$, however, the 'surface pressure' minimum is not bounded for the Baker vortex model and decreases with increasing swirl ratio as shown in figure 10 from -1.99 $\times \rho u_r(r_m, z_m)$ to -17.94 $\times \rho u_r(r_m, z_m)$ for S_{Baker} = 1 to 3 due to the term $-\frac{4.15{S_{Baker}}^2\left(ln\left(1+\bar{z}^2\right)\right)^2}{\left(1+\bar{r}^2\right)}$ (compare equation (*19*)). The effect of this on the 'surface pressure' distribution is masked in figure 10 due to normalising the pressure distribution additionally with $p(r,z_m)_{min}$ of the corresponding swirl ratio. This additional normalisation is applied to force all pressures to tend to -1 as r/R tends to 0. It is noted that some numerical and experimental data, e.g., Natarajan and Hangan (2012) and Haan et al. (2008), show that the surface pressure minimum decreases in magnitude with increasing swirl ratio which has been associated with a transition from a single-celled to a two-celled vortex. At present, although the Baker model is able to represent multiple cell tornadoes, this behaviour is not incorporated into the current paper.

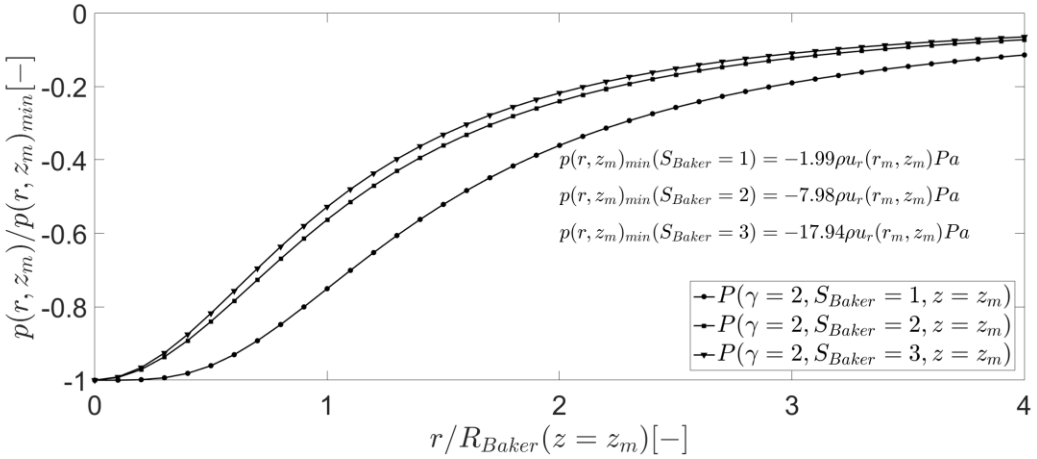

Figure 10: 'Surface pressure' distribution of the Baker vortex model for different swirl ratios (S_{Baker}).

The effect of the radial velocity profile on the 'surface pressure' is, not surprisingly, largest at the core radius (R_{Baker}) since this is where the radial velocity is maximum for $\gamma = 2$. When this term is normalised by the value of $p(r,z_m)_{min}$ for each corresponding swirl ratio, its magnitude changes and results in a different distribution of relative pressure (Figure 10). As a consequence, figure 10 shows that with increasing S_{Baker} the rate of change of pressure with increasing radial distance increases and hence, the smaller the vortex becomes. It needs to be mentioned here that this is only the case because the core radius (R_{Baker}) remains constant even though the swirl ratio changes. Due to the shape of the radial velocity component, differences in figure 10 are largest at $r / R_{Baker} (z = z_m) = 1$. The last term in equation (*19*) represents the effect of vertical advection of radial velocity on the 'surface pressure' distribution, i.e., $(-\frac{4ln(1+\bar{z}^2)(1-\bar{z}^2)}{(1+\bar{r}^2)^2(1+\bar{z}^2)^2})$. When $z = z_m$, this term reduces to zero.

3. Experimental methodology

In this section, the experimental methodology is presented, which was used to assess the ability (or otherwise) of the introduced vortex models to simulate flow and pressure characteristics obtained in a physical tornado-like vortex simulator.

3.1 Tornado-like vortex simulator

For this analysis, the University of Birmingham (UoB) tornado-like vortex generator (3m× 3m), which is based on the design by Ward (1972), is used (Figure 11). The generator consists of two chambers, a convergence chamber with height H_1 and diameter D_1 and a convection chamber with height H_2 and diameter D_2. The aspect ratio (a) is defined as the ratio of updraft radius (1/2 D_3) and convergence chamber height and therefore results in an aspect ratio of $a = 2$ for the configuration shown in Figure 11. Angular momentum is introduced by guide vanes around the

convergence chamber, which can be set to different angles. By changing the guide vane angle, the vorticity in the flow can be altered and different vortex structures can be generated.

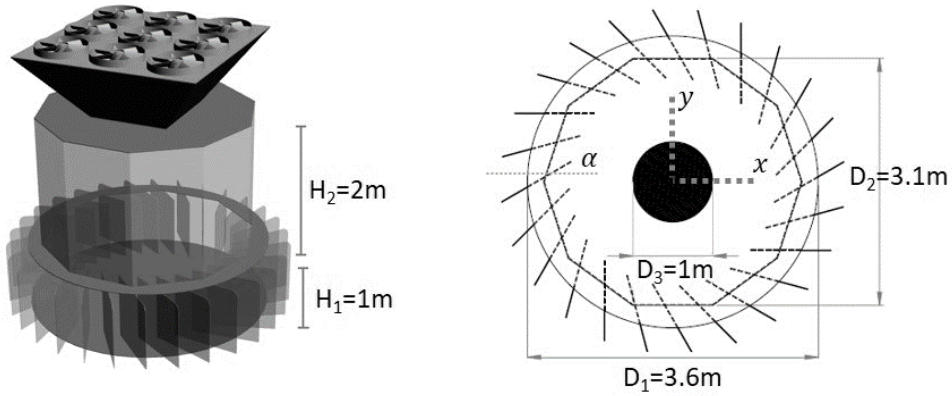

Figure 11: An illustration of the UoB tornado-like vortex generator.

The kinematic and dynamic similarity of the generated vortex is controlled by the Reynolds number, *Re,* (Eq. *22*) and the swirl ratio, *S,* (Eq. *23*).

$$Re = \frac{Q}{\boldsymbol{\nu}\, 0.5 D_3} \tag{22}$$

$$S = \frac{tan(\alpha)}{2a} \tag{23}$$

Here, Q is the flow rate through the simulator and ν is the kinematic viscosity of air. The guide vane angle, α, is the angle relative to the radial velocity component (Figure 11).

3.2 Measurement setup and data quality

Point velocity measurements were made with 100Hz using a Cobra Probe, which was mounted to a two-axis traverse system inside the simulator. This traverse system enabled the probe to be positioned with an accuracy of 1mm at nine heights (z) above the simulator's surface (0.01m, 0.05m, 0.10m, 0.15m, 0.20m, 0.25m, 0.30m, 0.40m, 0.50m, 0.60m) with a radial spacing of 0.025m from the centre of the simulator up to a radial distance of 0.60m. The size of the probe is less than 10^6 times smaller than the convergence chamber and the influence of the traverse system on the surface pressure measurements was found to be smaller than the experimental measurement uncertainty. The Cobra Probe can measure velocity data greater than 2m/s within a cone of influence of +/- 45°. These limitations can have a direct influence on the measured data. For example, if the recorded data quality (percentage of velocity samples of a measured time series which are >2m/s and have an angle of attack <+/- 45°) is less than 100% then this can introduce a bias in the calculated velocity vector – the lower the data quality the greater the potential bias. To minimize the bias in time averaged velocities, only those positions with a data quality of greater

than 80% were accepted for further analysis. This threshold is assumed to provide a suitable compromise between data quality and quantity.

The pressure distribution is measured with 100Hz on the ground plane along two perpendicular lines denoted x and y in figure 11. Surface pressure taps are distributed along these lines with a spacing of 0.05m from the simulator's centre up to a distance of 0.75m.

Different types of uncertainties have to be distinguished. The experimental uncertainty is a combination of uncertainties due to measuring a finite time series (statistical uncertainty), human error such as probe and guide vane angle positioning (repeatability) and the uncertainty of the measurement device itself.

3.2.1 Statistical uncertainty

The statistical uncertainty is a measure of uncertainty of the time average with respect to the unsteadiness of the flow or surface pressure field. Therefore, it is highly important to verify that the time average of a statistically, stationary stochastic process (such as a tornado) converges against the mean value of all possible realisations within the chosen measurement duration. In order to address the statistical uncertainty for this study, convergence tests were undertaken. For the convergence tests, time series were measured for a duration of 600 seconds. Running averages (*RA*) with increasing sampling durations (from 10 seconds – 600 seconds) were calculated and shown as envelope on the y-axis for the corresponding averaging time. For example, figures 12a and 12b show the convergence tests of the circumferential velocity component and surface pressure at the core radius of the lowest measurement height and at the centre of the simulator, respectively for $S = 0.69$.

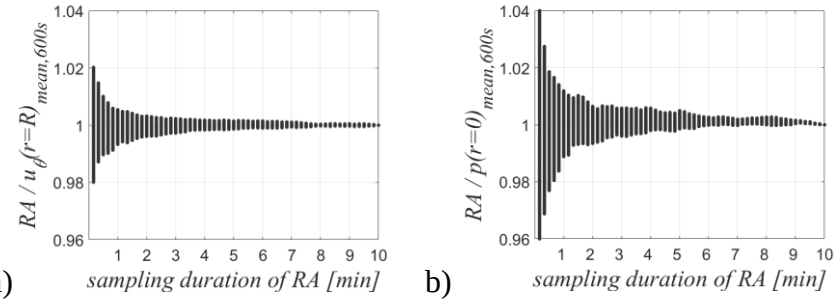

Figure 12: Convergence test of circumferential velocity (a) and surface pressure (b) for $S = 0.69$.

Figure 12 indicates that the uncertainty is reduced after a measurement duration of 80 seconds for velocities and 60 seconds for surface pressures. Hence, for this study, velocity and pressure measurements were conducted for a period of 80 and 60 seconds, respectively. The corresponding statistical uncertainties are shown in percentage of the time-average of the corresponding circumferential velocity component ($u_{\theta,mean,600s}$) and surface pressure ($p_{mean,600s}$) which was obtained after sampling for 600 seconds (Table 2).

Table 2: Statistical uncertainties of time-averaged velocity components and surface pressure.

	S = 0.14	*S = 0.30*	*S = 0.69*
	Velocity		
$u_\theta(r=R)_{,mean,600s}$ *[m/s]*	*5.31*	*9.39*	*10.51*
$u_\theta(r=R)_{uncertainty}$ *[%]*	*±1.94*	*±1.02*	*±0.54*
$u_r(r=R)_{uncertainty}$ *[%]*	*±5.96*	*±3.17*	*±0.52*
$w(r=R)_{uncertainty}$ *[%]*	*±1.21*	*±0.55*	*±0.25*
	Pressure		
$p(r=0)_{mean,600s}$ *[Nm^{-2}]*	*-136.30*	*-224.22*	*-164.44*
$p(r=0)_{uncertainty}$ *[%]*	*±26.75*	*±5.94*	*±1.16*

The 80-second time average of circumferential and vertical velocity components can be determined with an uncertainty of less than ±2% for all swirl ratios. Uncertainties of the radial velocity components are slightly larger with about ±6%, ±3% and ±0.5% for *S* = 0.14, *S* = 0.30 and *S* = 0.69, respectively.

For the surface pressure, 60 seconds of measurement time allow to determine the time-average to about ±27%, ±6% and ±1% for *S* = 0.14, *S* = 0.30 and *S* = 0.69, respectively. The uncertainty of surface pressure measurements at the centre of the simulator seems to be dependent on the swirl ratio, with lower uncertainties with increasing swirl ratio. This could be an indication for a more unstable vortex movement for the lowest swirl ratio compared to larger *S*. This behaviour cannot be observed in the uncertainties associated with the velocity measurements. A potential reason for this could be that the vortex movement occurs relatively close to the vortex centre where surface pressure gradients are relatively large, especially for the lowest swirl ratio, and for that reason, core radii positions are not that strongly affected by this behaviour.

3.2.2 Repeatability

The repeatability is the degree to which repeated measurements under unchanged boundary conditions show the same results. Surface pressure measurements and the radial profile of velocities in the lowest measurement height were repeated for five times for each swirl ratio. The measurement repeatability is analysed in form of a distribution of all possible differences of these repetitions. For example, figures 13a and 13b show the measurement repeatability distribution of circumferential velocity component and surface pressure for *S* = 0.69.

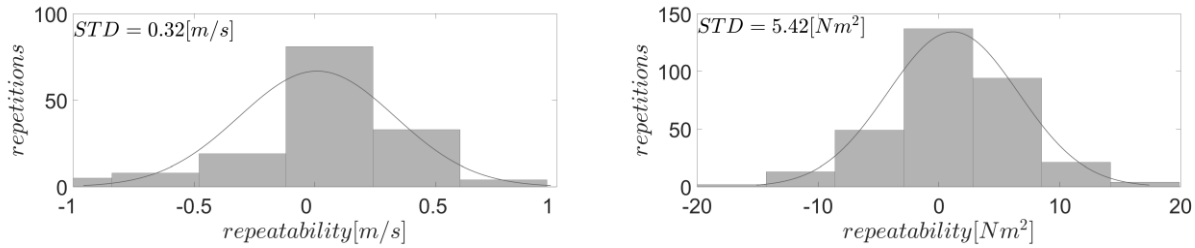

Figure 13: Distribution of the repeatability of circumferential velocity component (a) and surface pressure (b) for S = 0.69.

The standard deviation (*STD*) of the corresponding distributions was chosen as a representative measure to evaluate the repeatability, which is shown in table 3 for velocity components and surface pressures. Absolute values are given instead of percentages as these uncertainties are assumed to apply for all corresponding time averaged results. Similar to the statistical uncertainty, also table 3 shows that the repeatability of surface pressure measurements is dependent on the swirl ratio. For S = 0.14 and S = 0.30 the repeatability is not only dependent on the swirl ratio but also on the radial distance. For that reason, a repeatability dependent on r is introduced because a uniform value would highly underestimate the repeatability of measurement positions close to the vortex centre, and highly overestimate the repeatability for positions further away from the vortex centre (Table 3). No significant dependence on the radial distance was found for the repeatability of surface pressure measurements for S = 0.69 and all velocity measurements. Consequently, a uniform measurement repeatability independent from r is used for those cases (Table 3).

Table 3: Repeatability of time-averaged velocity components and surface pressures.

	S=0.14	*S=0.30*	*S=0.69*
	Velocity		
$u_{\theta,uncertainty}$ *[m/s]*	±*0.51*	±*0.44*	±*0.32*
$u_{r,uncertainty}$ *[m/s]*	±*0.46*	±*0.58*	±*0.22*
$W_{uncertainty}$ *[m/s]*	±*0.17*	±*0.16*	±*0.08*
	$P_{uncertainty}$ *[Nm^{-2}]*		
-0.05m < r < 0.05m	±*53.58*	±*21.74*	±*5.42*
r = ±*0.1m*	±*12.98*	±*17.34*	±*5.42*
r > 0.1m & r < -0.1m	±*1.86*	±*3.82*	±*5.42*

The low repeatability close to the vortex centre for S = 0.14 and S = 0.30 is not too surprising as the statistical uncertainty found at those positions (Table 2) is limiting the repeatability. Therefore, large uncertainties for S = 0.14 and S = 0.30 close to the vortex core can partly be explained by the large statistical uncertainty at these positions. Furthermore, these findings suggest that especially

positions close to the centre are sensitive to small variations in the boundary conditions such as guide vane angle positioning.

3.2.3 Device uncertainty

In this study, pressure transducers (HCLA12X5DB) with a typical uncertainty of $\pm$ 5 Nm^{-2} are used. The Cobra Probe is accurate within $\pm$ 0.5 m/s for the velocity vector up to a turbulence intensity of ~30%. Therefore, positions with a turbulence intensity greater than 30% are excluded from the analysis. Since the device uncertainty for the Cobra Probe is given for the velocity vector ($\vec{\boldsymbol{V}}$); the uncertainty of each velocity component needs to be calculated for each measurement position based on the obtained average of the corresponding velocity component. Equation 24 shows as an example the calculation of the device uncertainty for the circumferential velocity component at a certain position.

$$u_{\theta,uncertainty} = 0.5 \left\langle \frac{|u_\theta|}{\vec{V}} \right\rangle \tag{24}$$

3.2.4 Experimental uncertainty

The associated experimental uncertainty of velocity and surface pressure measurements, which is shown as envelope in later figures is based on a combination of the repetition uncertainty (shown in table 3) and the device uncertainty.

4. Comparison

In this section, flow field and surface pressure data for three different swirl ratios (S = 0.14, S = 0.30, and S = 0.69) are analysed and the capability of the vortex models to replicate the experimental results is evaluated.

4.1. The flow structure

In order to address the complex nature of the analysed flow fields, the 3-D velocity fields obtained for *S = 0.14*, *S = 0.30* and *S = 0.69* are shown in figure 14. Also shown are results of selected analytical vortex models, which for the sake of brevity are not repeated for all swirl ratios. The 'viscosity' parameter for the Burgers-Rott and Sullivan model is assumed to be v=0.05 m^2s^{-1}. However, for the analysis presented in figure 14b, the actual 'viscosity' value is not that crucial because the focus of this analysis lies rather on the flow structure than on the actual velocity magnitude, which is affected by the 'viscosity'.

Velocity components are normalised by the maximum circumferential velocity ($u_{\theta,max}$) of the corresponding swirl ratio. Radial/vertical distances are normalised by the corresponding core radius (R). All of the simplified models presented in section 2 assume a height independent core radius and all vortex models besides the Baker vortex model assume a height independent $u_{\theta,max}$. For this reason, velocity components are normalised by the height average of the maximum circumferential velocity ($u_{\theta,max,average}$) of the corresponding swirl ratio (Eq. 25) and radial/vertical distances are normalised by the corresponding height averaged core radius ($R_{average}$, Eq. 26). The use of averaged quantities is considered to give the best indication of a representative core radius and maximum circumferential velocity for all heights.

$$u_{\theta,max,average} = \frac{1}{N}\sum_{i=1}^{N} u_{\theta,max}(z)_i \quad (25)$$

$$R_{average} = \frac{1}{N}\sum_{i=1}^{N} R(z)_i \quad (26)$$

where N is the number of measurement heights.

A further degree of normalisation is undertaken to aid visual comparisons, i.e., each height (radial distance) is normalised by the corresponding maximum of $z/R_{average}$ ($r/R_{average}$) for each swirl ratio – the actual maxima used are given in the figure captions. Experimentally obtained $R_{average}$ and $u_{\theta,max,average}$ (shown in figure 15) are used to calculate the flow field of the Rankine, Burgers-Rott, Sullivan and Baker vortex models for corresponding swirl ratios. Due to the restrictions when measuring with the Cobra probe, the velocity field close to the vortex centre for all swirl ratios and near the surface at larger radial distances for $S = 0.14$ could not be captured. Inside the vortex core ($r < R_{average}$), velocity vectors are only shown at positions where absolute values of time averaged radial and vertical velocities are larger than the corresponding measurement uncertainty. Hence, only positions for which a clear directionality can be defined are presented in figure 14.

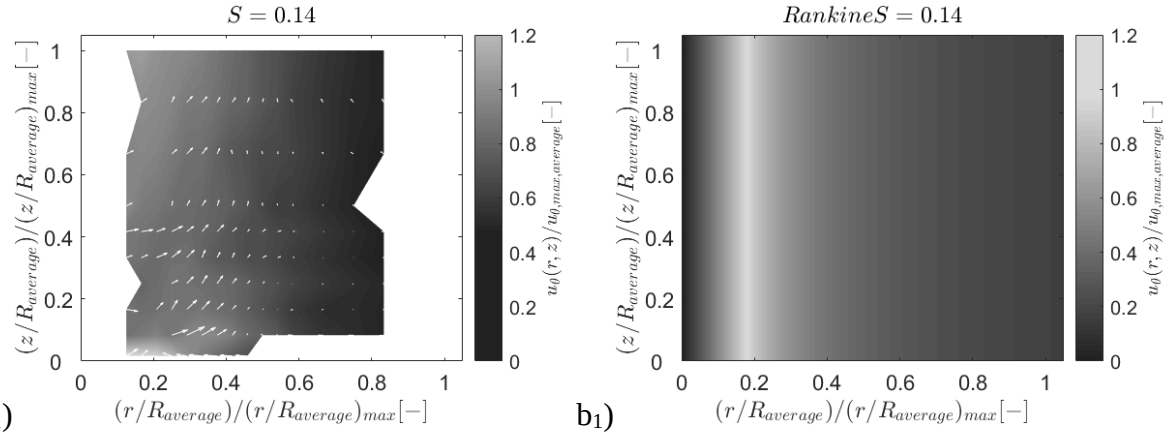

a$_1$) b$_1$)

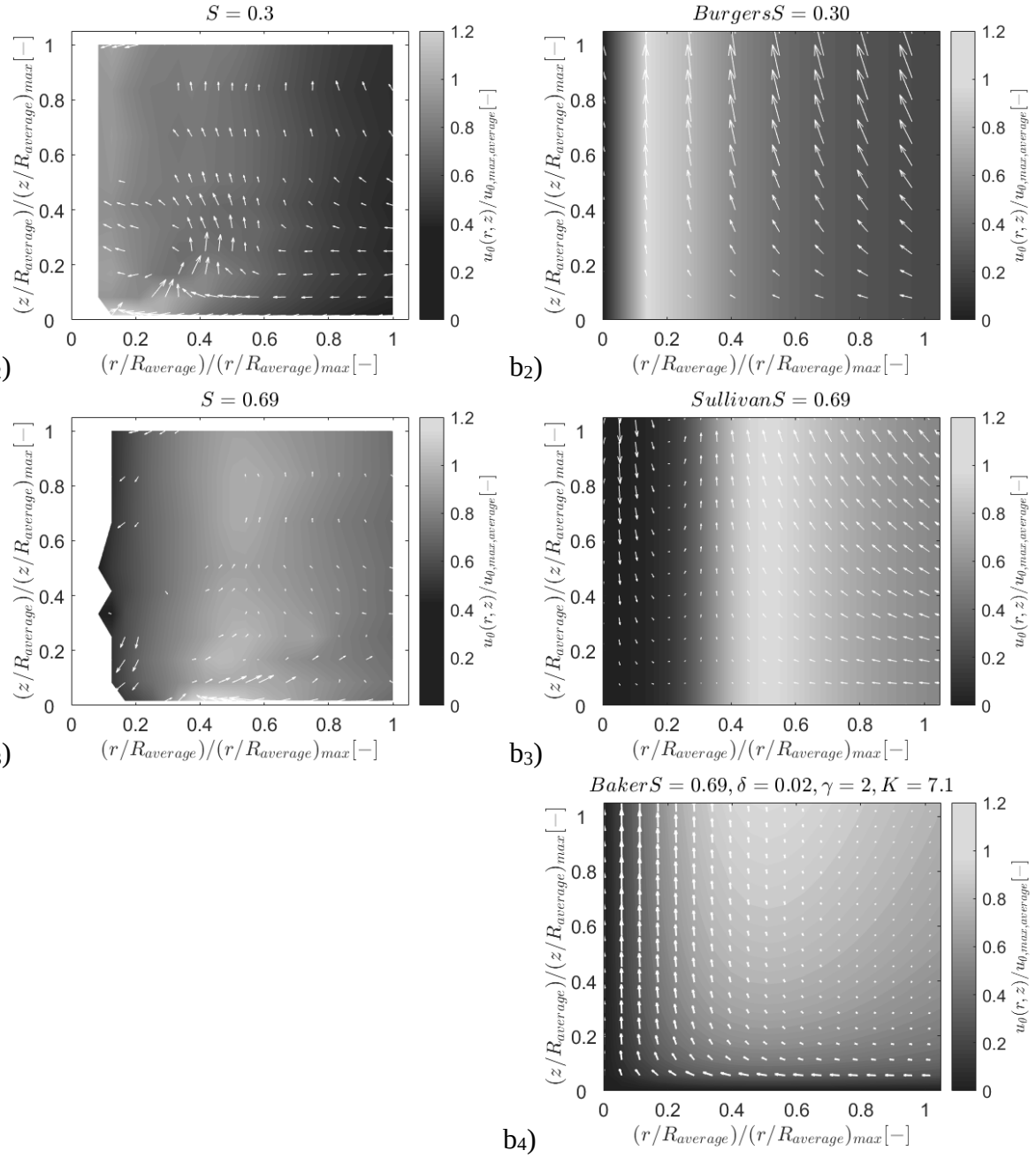

Figure 14: Experimental results of the 3-D velocity field are shown in a_1 (S = 0.14), a_2 (S = 0.30) and a_3 (S = 0.69). Corresponding results of Rankine, Burgers-Rott, Sullivan and Baker vortex models are shown in b_1, b_2, b_3 and b_4, respectively. The normalised circumferential velocity component is shown as contour and radial and vertical velocity components are shown as 2-D vector field. To normalise heights and distances, maximum values of experimentally obtained $(z/R_{average})_{max}$ and $(r/R_{average})_{max}$ are used. For S = 0.14, S = 0.30 and S = 0.69 $(r/R_{average})_{max}$ = $(z/R_{average})_{max}$ = 5.58, 7.27 and 1.97, respectively.

In general, experimentally obtained flow characteristics reveal much more complex flow patterns compared to the vortex models (Figure 14). The measured circumferential velocity component for all swirl ratios increases towards the core radius and reaches the overall maximum close to the surface. Furthermore, a strong decrease in circumferential velocity can be observed with height in

the lower heights for all swirl ratios (Figure 14a). The circumferential velocity components of Rankine, Burgers-Rott and Sullivan vortex models (Figure $14b_1$, Figure $14b_2$, and Figure $14b_3$) are not a function of height and consequently, cannot represent the height dependence found in the simulator (Figure 14a). The circumferential velocity of the Baker vortex model is height dependent and increases with increasing height from the ground (Figure $14b_4$), which is also not obtained experimentally. It can be noticed in figure 14a that for all swirl ratios, a strong inflow can be detected close to the surface, up to the position where the overall maximum circumferential velocity occurs. At this position, the radial velocity drops drastically and the vertical velocity increases significantly.

Contrary to what may be expected, Figure $14a_1$, shows a radial outflow from the vortex centre. However, this is supported by the work of Mishra et al., (2008) and Haan et al., (2008), where tentative evidence of a radial outflow close to the vortex centre can be inferred. Various possible reasons for this behaviour (including vortex core unsteadiness with respect to height) could be inferred, however, firm conclusions as to why this may be the case cannot, at present, be drawn.

With increasing swirl ratio (S = 0.69), a downdraft is detected close to the centre of the simulator (Figure $14a_3$). This flow structure is expected for a two-celled vortex (see Sullivan vortex model, Figure $14c_3$). However, the downdraft is directed slightly towards the simulator's centre which was also observed by Haan et al., (2008) for a high swirl ratio. The lack of detailed, fine scale, experimental data at the centre of the vortex make further conclusions difficult.

Due to non-existing radial and vertical velocity components, this behaviour cannot be represented with the Rankine vortex model (Figure $14b_1$). Notwithstanding the more complex structure of Burgers-Rott, Sullivan, and Baker vortex models, the measured flow pattern are far more complex than the analytical models would suggest.

A more detailed analysis of the flow field can be found in figures 15 - 17 illustrating the circumferential, radial and vertical velocity components for z = 0.01m, z = 0.10m, z = 0.20m and z = 0.40m, for S = 0.14 (a), S = 0.30 (b) and S = 0.69 (c).

Experimentally obtained results for $\overline{u_\theta}$ (Figure 15) show that for all swirl ratios, the overall maxima of $\overline{u_\theta}$ occurs at the lowest measurement height (z=0.01m, Figure 15). The distribution of circumferential velocity components at greater heights is relatively uniform and differences lie within the experimental uncertainty (Figure 15). The lowest height reveals an entirely different flow structure compared to the rest of the generated vortex. This suggests a similar vertical profile of circumferential velocity components as observed by Kosiba and Wurman (2013). Figure 15 also outlines differences in the circumferential velocity profile for different swirl ratios. Figure 15 shows that $u_{\theta,max,average}$ increases with increasing swirl ratio from 3.65 – 8.75m/s. Also, the core radius increases with increasing swirl ratio from 0.11 – 0.31m. Results obtained for S = 0.30 do

not follow this trend and reveal an averaged core radius of 0.08m, which is smaller than the one observed for S = 0.14. However, it is worth noting that the difference between $R_{average}$ for S = 0.14 and S = 0.30 is ~0.03m. This difference is within the experimental uncertainty of determining $R_{average}$ and would therefore be masked when taking the uncertainty of determining $R_{average}$ into account, which is approximately $\pm$ 0.02m.

In general, the Rankine, Burgers-Rott and Sullivan vortex models appear to underestimate the trend of $\overline{u_\theta}$ for S = 0.14 (Figure 15a), although the differences are close to or within the experimental uncertainty in most cases. However, the Baker model appears to predict the trend reasonably well for this swirl ratio. All models appear to fail to capture the distribution of $\overline{u_\theta}$ at relatively large values of S (Figure 15b).

Inside the vortex core, a comparison between experimentally obtained results and vortex models is difficult due to the lack of good experimental data for S = 0.14 and S = 0.30 (Figure 15a and Figure 15b). The circumferential velocity component of the Burgers-Rott and Baker vortex model match the experimental data obtained for S = 0.69 (Figure 15c). Results from the Rankine and Sullivan vortex model, again underestimate the magnitude of obtained circumferential velocities for the highest swirl ratio.

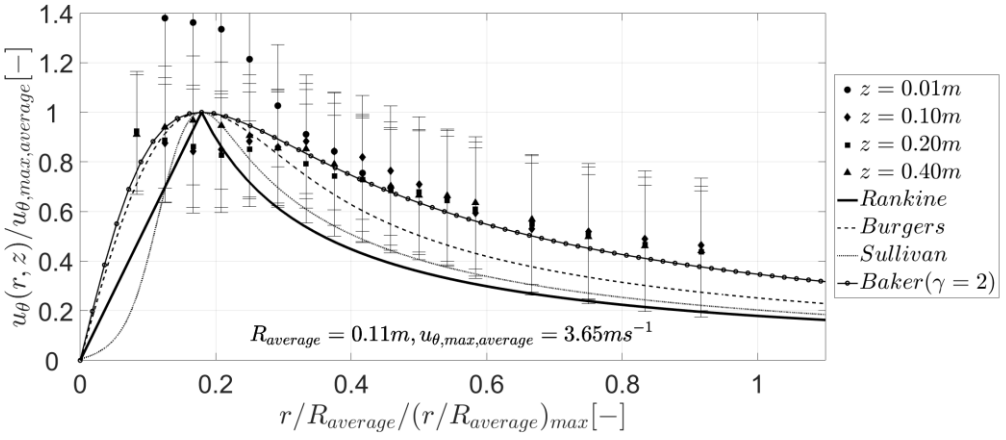

a)

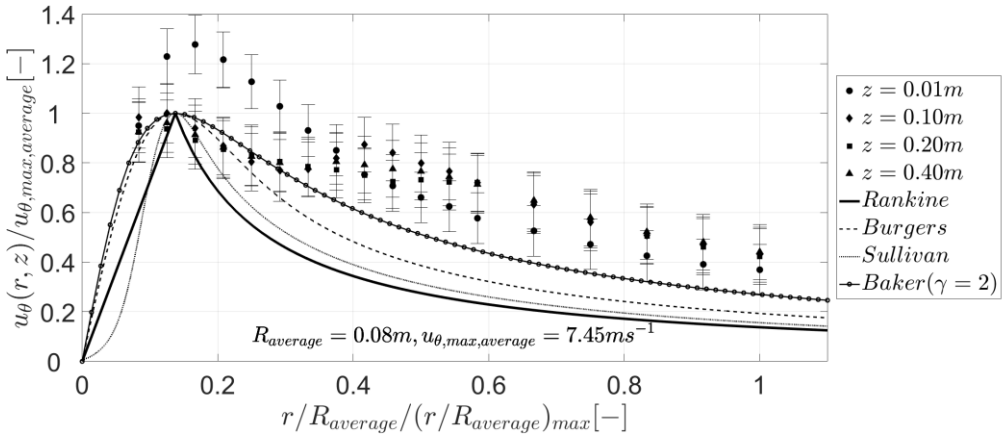

b)

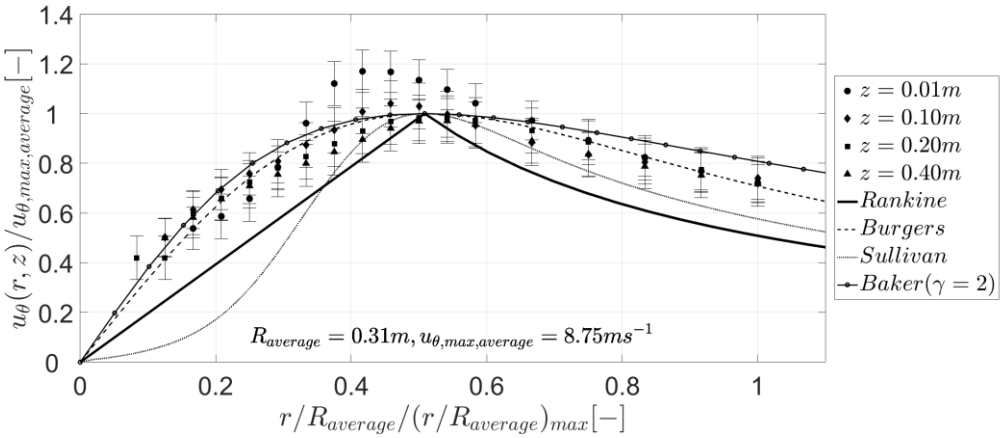

c)

Figure 15: Measured circumferential velocity component for S = 0.14 (a), S = 0.30 (b) and S = 0.69 (c). Additionally, results of the circumferential velocity component of Rankine, Burgers-Rott, Sullivan, and Baker vortex models are shown. To normalise the radial distance, maximum values of experimentally obtained $(r/R_{average})_{max}$ are used. For S = 0.14, S = 0.30 and S = 0.69 $(r/R_{average})_{max} = (z/R_{average})_{max}$ = 5.58, 7.27 and 1.97, respectively.

Figure 16 illustrates the radial distribution of $\overline{u_r}$ for z = 0.01m, z = 0.10m, z = 0.20m and z = 0.40m. Additionally a height average is calculated and shown for all velocities obtained for z > 0.01m. It needs to be mentioned here that the swirl ratio (S) defined in equation *23* is, unlike the definition adopted in the Baker vortex model (S_{Baker}), solely a function of the tornado generator characteristics. For that reason, values of S and S_{Baker} differ for the same flow field in the following figures. As illustrated in figure 16a and 16b, the Baker model fits the data obtained reasonably well close to the surface, whereas the Sullivan and Burgers-Rott vortex model are a better fit for experimental data obtained in greater heights. This is perhaps not too surprising given the assumptions embedded in the models. However, for the largest swirl ratio (Figure 16c), the Baker model only represents the trend in the lowest height for normalised radial distances greater than 0.6, whereas the Sullivan model performs better for the lowest height and for lower normalised radial distances.

For *S = 0.14*, the radial outflow inside the vortex core suggests the structure of a (limited height) two-celled vortex. Thus, in general, the height averaged structure of $\overline{u_r}$ appears to be reasonably represented by the Sullivan vortex model (Figure 16a). Even though one feature of a two-celled vortex is present for *S = 0.14*, the vertical downdraft suggested by the Sullivan vortex model at the vortex centre was not capture (Figure 17a). For the vertical velocity component obtained with S = 0.14, none of the vortex models is capable of replicating the maximum updraft just outside the vortex core (Figure 17a). However, for larger radial distances, results of Burgers-Rott and Sullivan vortex model can be used to reproduce height averaged vertical velocities (Figure 17a). Certainly, it needs to be mentioned here that for this case, the vortex models fail to replicate the complex behaviour observed experimentally. Although there are only few positions available for a comparison in the lowest height, radial and vertical velocity component of the Baker vortex model are in good agreement with the experimental data (Figure 16a and Figure 17a).

For S = 0.30, radial velocities are mainly directed towards the vortex centre (radial inflow). The magnitude of radial velocities in greater heights z > 0.01m is relatively low compared to radial velocities obtained in the lowest height ($z=0.01m$). The best fit for this 'single-celled' flow behaviour is achieved with the Burgers-Rott vortex model with a relatively low 'viscosity' parameter ($\nu=0.0015m^2s^{-1}$) to minimise the increase of radial inflow from the vortex centre to larger radial distances. Similar to the vertical velocity component found for S = 0.14, also here the maximum updraft outside the vortex core (Figure 17b) cannot be replicated by any of the introduced vortex models. However, for larger radial distances the Burgers-Rott vortex model can be used to model the height averaged behaviour (Figure 17b). Nevertheless, the complex vertical flow structure cannot be captured. Radial and vertical velocity component of the Baker vortex model on the other hand are in good agreement with the experimental data for $z=0.01m$ (Figure 16b and Figure 17b).

For S = 0.69, radial velocities (Figure 16c) are found to be directed inwards, towards the vortex centre (radial inflow), even though a downdraft close to the vortex centre is found (Figure 17c). In terms of vortex models, this means that the radial velocity shows a 'single-celled' behaviour with radial inflow (Burgers-Rott and Baker), whereas the vertical velocity illustrates a 'two-celled' structure with downdraft (Sullivan). None of the presented vortex models is capable of representing both of the observed flow patterns. For S = 0.69, the flow field obtained is far more complex than the assumed flow structure of a single or a double-celled vortex. In this case, the flow reveals a 'multi-celled' structure with a weak radial inflow and updraft outside the core vortex and relatively strong radial inflow and downdraft inside the core vortex (Figure 16c and Figure 17c).

For radial and vertical velocity components of S = 0.69, an attempt is shown to use Sullivan and Baker vortex model to replicate some of the flow patterns observed in the lowest height (z = 0.01m). For the radial velocity component in the lowest height (Figure 16c), the Baker vortex model captures the radial inflow outside the vortex core but overestimates velocities inside the vortex core. The decrease in radial inflow around the core radius can be replicated with the Sullivan vortex model, however, close to the vortex centre, the Sullivan vortex model is not able to replicate the flow field and also for larger radial distances the Sullivan vortex model fails due to its increasing radial velocity component with increasing radial distance (Figure 16c).

For the vertical velocity (Figure 17c), the Sullivan vortex model can represent parts of the observed results. By means of the shape parameter, b, the downdraft region around the vortex centre of the Sullivan vortex model can be extended in the radial direction so that for b = 12, results of the Sullivan model show some similarity with the increase in radial inflow from the vortex core towards the vortex centre (Figure 17c). However, increasing, b, also results in an increasing downdraft at the core radius, which for S = 0.69 is highly overestimated. The Baker vortex model

is not able to replicate the downdraft close to the vortex centre and the relatively strong vertical updraft around the core radius.

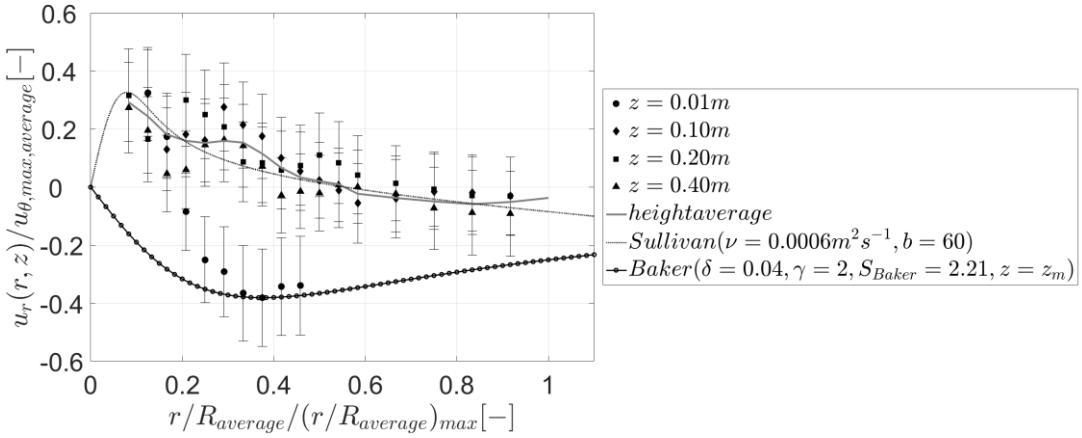

a)

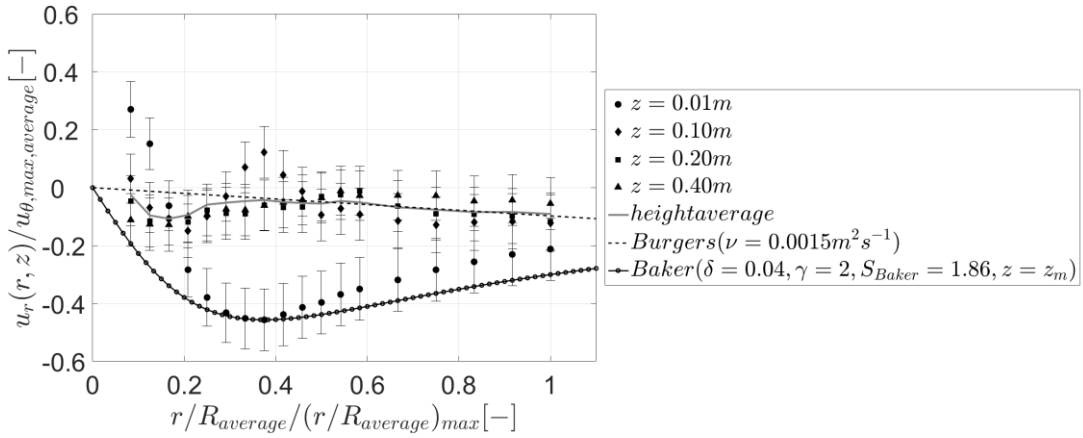

b)

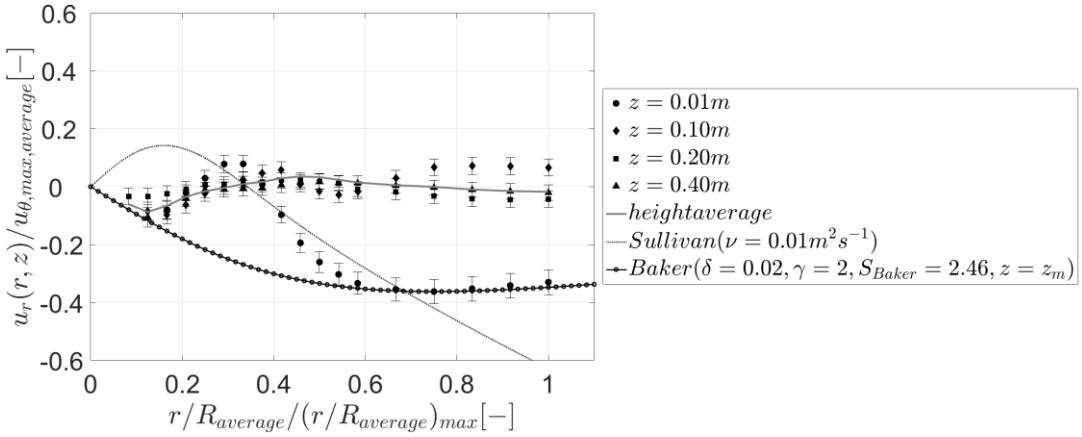

c)

Figure 16: Measured radial velocity component for S = 0.14 (a), S = 0.30 (b) and S = 0.69 (c). Additionally, results of the radial velocity component of Burgers-Rott (b) and Sullivan vortex model (a and c) are shown. Results of the Baker vortex model are shown for the lowest height (z = 0.01). To normalise the radial distance, maximum values of experimentally obtained $(r/R_{average})_{max}$ are used. For S = 0.14, S = 0.30 and S = 0.69 $(r/R_{average})_{max} = (z/R_{average})_{max}$ = 5.58, 7.27 and 1.97, respectively.

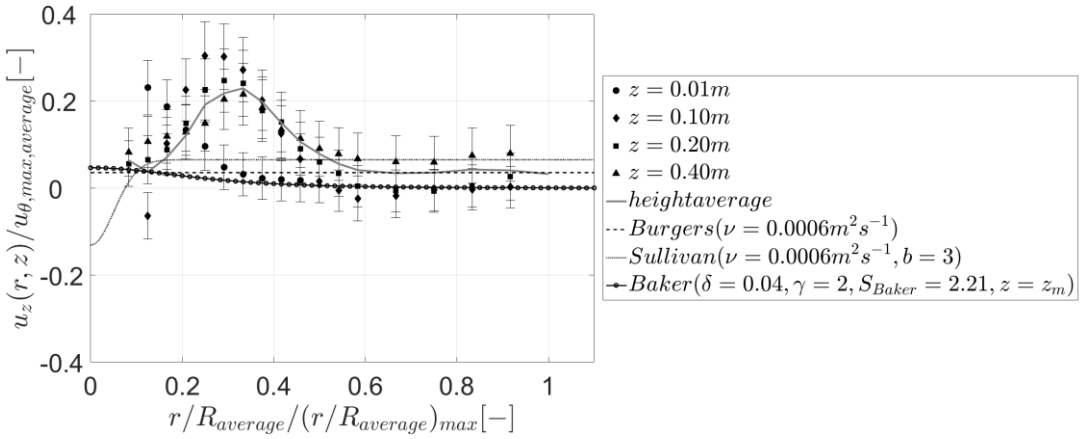

a)

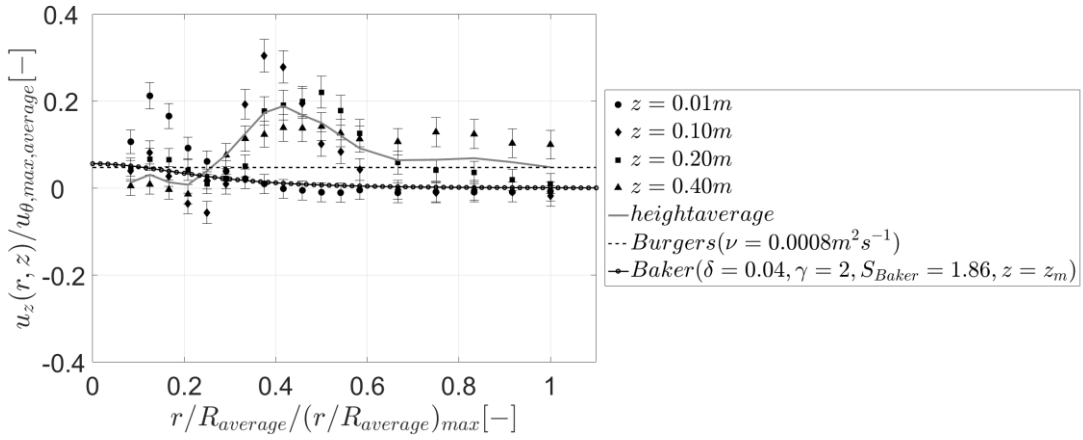

b)

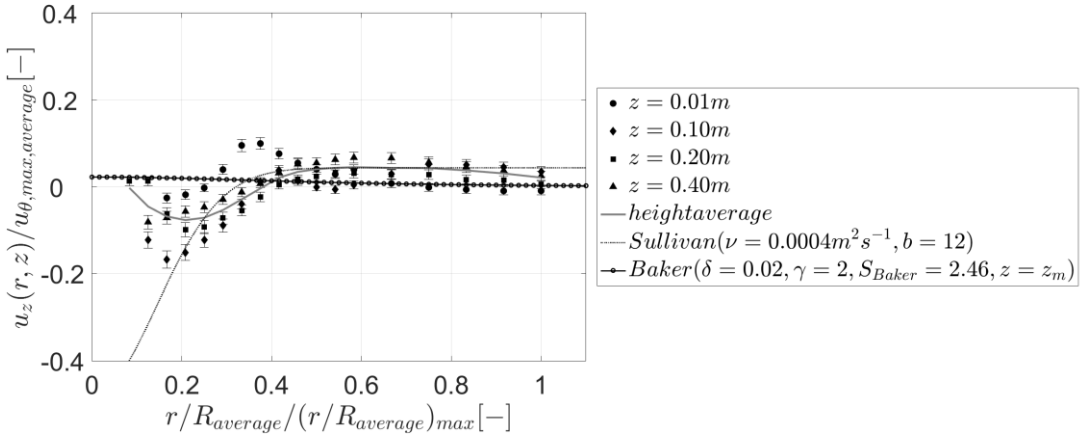

c)

Figure 17: Measured vertical velocity component for *S* = 0.14 (a), *S* = 0.30 (b) and *S* = 0.69 (c). Additionally, results of the vertical velocity component of Burgers-Rott (a and b) and Sullivan vortex model (a and b) are shown. Results of the Baker vortex model are shown for the lowest height (z = 0.01). To normalise the radial distance, maximum values of experimentally obtained $(r/R_{average})_{max}$ are used. For *S* = 0.14, *S* = 0.30 and *S* = 0.69 $(r/R_{average})_{max}$ = $(z/R_{average})_{max}$ = 5.58, 7.27 and 1.97, respectively.

4.2 Surface pressure distribution

Figure 18 and figure 19 show the surface pressure distribution for $S = 0.14$, $S = 0.30$, and $S = 0.69$. Additionally, the surface pressure distributions of the Rankine, Burgers-Rott and Sullivan vortex models are illustrated in figure 18 and results of the Baker vortex model are shown in figure 19.

Looking at figures 18 and 19, it could be concluded that differences in the measured surface pressure distribution depend significantly on the swirl ratio. As expected, the smallest vortex shows the fastest increase in surface pressure from the vortex centre towards larger radial distances ($S = 0.14$). The slope of the surface pressure change is determined by the measured surface pressure distribution but also affected by the normalisation of radial distances. This means, for the same surface pressure distribution, a larger core radius leads to a surface pressure distribution, which is increasing faster from the vortex centre towards larger radial distances. For that reason, the surface pressure distribution of $S = 0.30$ and $S = 0.60$ reveal an unexpected behaviour. The surface pressure distribution obtained with $S = 0.69$ displays a faster increase of surface pressure with increasing radial distance compared to the pressure distribution measured with $S = 0.30$. This can be explained by the relatively small averaged core radius for $S = 0.30$ ($R_{average,\,(S=0.30)} = 0.08$m) compared to $R_{average}$ of $S = 0.14$ ($R_{average,\,(S=0.14)} = 0.11$m) and $S = 0.69$ ($R_{average,\,(S=0.69)} = 0.31$m).

To avoid an unphysical decrease in surface pressure with increasing radial distance, the 'viscosity' parameter of the Sullivan vortex model is chosen to be zero and for the Burgers-Rott vortex model, v and $\bar{a}$ are adjusted for each swirl ratio to guaranty a physically reasonable surface pressure increase with increasing radial distance (Figure 18).

The largest differences in the surface pressure distribution of the vortex models is found close to the vortex centre, whereas largest differences in the experimental surface pressure data for the three different vortices are found outside the vortex core (Figure 18). The surface pressure distributions of the Rankine and Burgers-Rott vortex models are in good agreement with the experimental data for $S = 0.69$ (Figure 18), albeit the Burgers-Rott vortex model fails for larger radial distances due to a physically unrealistic decrease in surface pressure, which is explained in section 2.8. Also, the Sullivan vortex model shows good agreement for this swirl ratio ($S = 0.69$) but only for larger radial distances. Close to the vortex centre, the Sullivan vortex model underestimates experimental results due to its two-celled structure (Figure 18). Even though a downdraft is present close to the vortex centre for $S = 0.69$, the effect of it is not visible in the experimentally obtained surface pressure distribution.

All three solutions of the Baker vortex model match the experimental surface pressure for S = 0.30 the best (Figure 19). The swirl ratio of the Baker vortex model (S_{Baker}) is responsible for differences in the surface pressure distribution. However, differences in S_{Baker} for the three analysed vortices are too small to cause significant differences in the surface pressure distribution (Figure 19). To allow a more flexible surface pressure model, the shape parameter, γ, in the Baker model needs to be treated as a variable when deriving the static pressure distribution (Eq. 19). This would allow

different core radii (R_{Baker}) and also different shapes of the surface pressure distribution to be generated. However, in this work, the surface pressure equation for the Baker vortex model (Eq. 19) assumes a shape parameter of $\gamma=2$. Consequently, the calculated surface pressure distributions shown in figure 19 assume a constant core radius (R_{Baker}) for all three vortices. For this reason, the surface pressure distributions of the Baker vortex model does not allow an accurate representation of the experimentally obtained surface pressure profiles.

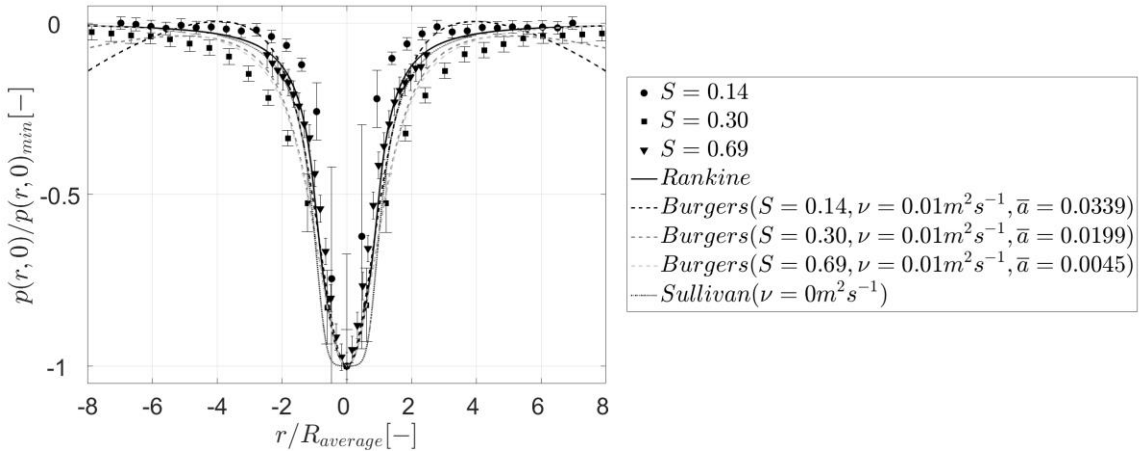

Figure 18: Measured surface pressure distribution for S=0.14 (a), S=0.30 (b), and S=0.69 (c) and surface pressure of Rankine, Burgers-Rott, and Sullivan vortex model.

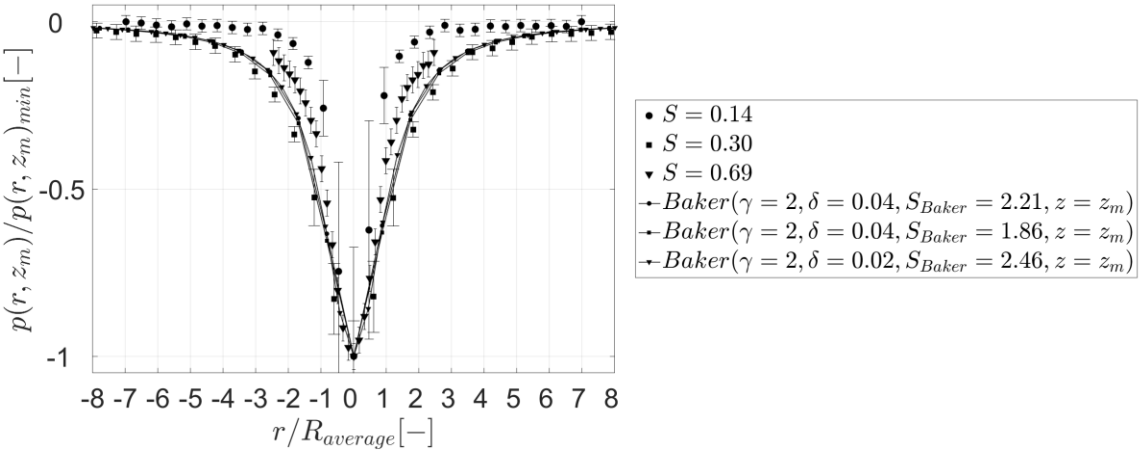

Figure 19: Measured surface pressure distribution for S=0.14 (a), S=0.30 (b), and S=0.69 (c) and surface pressure of the Baker vortex model.

5. Conclusion

Based on this analysis, the following main conclusions can be drawn:

- Despite the simplicity of all the models examined, it has been shown that this area of research is highly complex, largely due to the interpretation of the different parameters involved.
- The Burgers-Rott and Sullivan vortex models are able to replicate some parts of the flow field. However, parameters, which need to be chosen to make the model results fit the experimental data ($\nu, \bar{a}$ and b) differ for surface pressure and different velocity components of the same vortex.
- The Baker vortex model seemed to be the best model to replicate the radial inflow close to the ground. However, it fails for larger heights over the range tested.
- Measured flow pattern are far less structured and organised than the pattern suggested by any of the vortex models. Consequently, none of the presented models can be used to represent the three dimensional vortex structures of experimentally generated tornado-like vortices.
- Rankine, Burgers-Rott and Sullivan vortex model are able to replicate the surface pressure distribution of one of the analysed vortices (S = 0.69) but due to their limitations, these models are not adequate enough to replicate a variety of differently shaped pressure distributions.
- The Baker vortex model with a shape parameter of $\gamma = 2$ allows the representation of the surface pressure distribution obtained for (S = 0.30). A more general expression for the surface pressure is required to represent experimental data for all three vortices.

References

Alekseenko, S.V., Kuibin, P.A., Okulov, V.L., 2007. Theory of Concentrated Vortices. Springer Berlin Heidelberg New York. ISBN 978-3-540-73376-8. http://doi.org/10.1007/978-3-540-73376-8

Alexander, C.R. and Wurman J.M., 2008. Updated mobile radar climatology of supercell tornado structures and dynamics. 24th Conference on Severe Local Storms, Savannah, GA.

Baker C.J. and Sterling M., 2017. Modelling wind fields and debris flight in tornadoes. Journal of Wind Engineering and Industrial Aerodynamics 168, 312-321. https://doi.org/10.1016/j.jweia.2017.06.017

Batterson J.W., Maicke B.A., Majdalani J., 2007. Advancements in Theoretical Models of Confined Vortex Flowfields. Defense Technical Information Center, University of Tennessee Space Institute, Tullahoma, TN 37388.

Bech J., Gayà M., Aran M., Figuerola F., Amaro J., Arús J., 2009. Tornado damage analysis of a forest area using site survey observations, radar data and a simple analytical vortex model. Atmospheric Research 93, 118–130. https://doi.org/10.1016/j.atmosres.2008.10.016

Bloor, M.I.G., Ingham, D.B., 1987. The flow in industrial cyclones. Journal of Fluid Mechanics 178, 507-519. https://doi.org/10.1017/S0022112087001344

Brown, R.A., Wood, V.T., 2004. Comparisons of Doppler velocity tornadic vortex signatures with signatures from model vortices. 22nd Conference on Severe Local Storms, Anonymous Hyannis, MA.

Burgers, J.M., 1948. A Mathematical Model Illustrating the Theory of Turbulence. Advances in Applied Mechanics 1, 171-199. https://doi.org/10.1016/S0065-2156(08)70100-5

Church, C.R., Snow, J.T., Baker, G.L., Agee, E.M., 1979. Characteristics of Tornado-Like Vortices as a Function of Swirl Ratio: A Laboratory Investigation. Journal of the Atmospheric Sciences 36, 1755-1776. https://doi.org/10.1175/1520-0469(1979)036<1755:COTLVA>2.0.CO;2

Davies-Jones, R. and Kessler, E., 1974. Tornadoes. Weather and Climate Modification, W. N. Hess, Ed., Wiley, 552-595.

Davies-Jones, R., Trapp, R.J., Bluestein, H.B., 2001. Tornadoes and Tornadic Storms. Meteorological Monographs 50, 167-222. https://doi.org/10.1175/0065-9401-28.50.167

Gillmeier, S., Sterling, M., Hemida, H., 2016. An Analysis of the Influence of a Tornado Generator's Geometry on the Flow Field. 8th International Colloquium on Bluff Body Aerodynamics and Applications. Boston, Massachusetts, USA.

Haan Jr, F.L., Sarkar, P.P., Gallus, W.A., 2008. Design, construction and performance of a large tornado simulator for wind engineering applications. Engineering Structures 30, 1146-1159. https://doi.org/10.1016/j.engstruct.2007.07.010

Hashemi Tari, P., Gurka, R., Hangan, H., 2010. Experimental investigation of tornado-like vortex dynamics with swirl ratio: The mean and turbulent flow fields. Journal of Wind Engineering and Industrial Aerodynamics 98, 936-944. https://doi.org/10.1016/j.jweia.2010.10.001

Hoecker, W.H., 1960. Wind speed and air flow patterns in the Dallas tornado of April 2, 1957. Monthly Weather Review 88, 167-180. https://doi.org/10.1175/1520-0493(1960)088<0167:WSAAFP>2.0.CO;2

Karstens, C.D., Samaras, T.M., Lee, B.D., Gallus Jr., W.A., Finley, C.A., 2010. Near-Ground Pressure and Wind Measurements in Tornadoes. Monthly Weather Review 138, 2570-2588. https://doi.org/10.1175/2010MWR3201.1

Kilty, K.T., 2005. Steady-state tornado vortex models. http://www.kilty.com/pdfs/models.pdf (last accessed 08/06/2017).

Kim, Y.C., Matsui, M., 2017. Analytical and empirical models of tornado vortices: A comparative study. Journal of Wind Engineering and Industrial Aerodynamics 171, 230-247. https://doi.org/10.1016/j.jweia.2017.10.009

Kosiba, K., Wurman, J., 2010. The Three-Dimensional Axisymmetric Wind Field Structure of the Spencer, South Dakota, 1998 Tornado. Journal of the Atmospheric Sciences 67, 3074-3083. https://doi.org/10.1175/2010JAS3416.1

Kosiba, K., Wurman, J., 2013. The Three-Dimensional Structure and Evolution of a Tornado Boundary Layer. Weather and Forecasting 28, 1552-1561. https://doi.org/10.1175/WAF-D-13-00070.1

Kuo, H.L., 1971. Axisymmetric Flows in the Boundary Layer of a Maintained Vortex. Journal of the Atmospheric Sciences 28, 20-41. https://doi.org/10.1175/1520-0469(1971)028<0020:AFITBL>2.0.CO;2

Lee, J., Samaras, T., Young, C. R., 2004. Pressure measurements at the ground in an F-4 tornado. 22nd Conference on Severe Local Storms, Anonymous Hyannis, MA.

Lewellen, W.S., 1993. Tornado Vortex Theory, The Tornado: Its Structure, Dynamics, Prediction, and Hazards. Geophys. Monogr 79, edited by C. Church et al., pp. 19-39, AGU, Washington, D. C. https://doi.org/ 10.1029/GM079

Lewellen, W.S., Lewellen, D.C., Sykes, R.I., 1997. Large-Eddy Simulation of a Tornado's Interaction with the Surface. Journal of the Atmospheric Sciences 54, 581-605. https://doi.org/10.1175/1520-0469(1997)054<0581:LESOAT>2.0.CO;2

Liu, Z., Ishihara, T., 2016. Study of the effects of translation and roughness on tornado-like vortices by large-eddy simulations. Journal of Wind Engineering and Industrial Aerodynamics 151, 1-24. https://doi.org/10.1016/j.jweia.2016.01.006

Mishra, A.R., James, D.L., Letchford, C.W., 2008. Physical simulation of a single-celled tornado-like vortex, Part A: Flow field characterization. Journal of Wind Engineering and Industrial Aerodynamics 96, 1243-1257. https://doi.org/10.1016/j.jweia.2008.02.063

Natarajan, D., 2011. Numerical Simulation of Tornado-like Vortices. The University of Western Ontario Electronic Thesis and Dissertation Repository.

Natarajan, D., Hangan H., 2012. Large eddy simulations of translation and surface roughness effects on tornado-like vortices. Journal of Wind Engineering and Industrial Aerodynamics 104-106, 577-584. https://doi.org/10.1016/j.jweia.2012.05.004

Nolan, D.S., Dahl, N.A., Bryan, G.H., Rotunno, R., 2017. Tornado Vortex Structure, Intensity, and Surface Wind Gusts in Large-Eddy Simulations with Fully Developed Turbulence. Journal of the Atmospheric Sciences 74, 1573-1597. https://doi.org/10.1175/JAS-D-16-0258.1

Rankine, W.J.M., 1882. A Manual of Applied Physics. 10th ed. Charles Griff and Co. 663 pp.

Refan, M., Hangan, H., 2016. Characterization of tornado-like flow fields in a new model scale wind testing chamber. Journal of Wind Engineering and Industrial Aerodynamics 151, 107-121. https://doi.org/10.1016/j.jweia.2016.02.002

Refan, M., Hangan, H., Wurman, J., 2014. Reproducing tornadoes in laboratory using proper scaling. Journal of Wind Engineering and Industrial Aerodynamics 135, 136-148. https://doi.org/10.1016/j.jweia.2014.10.008

Refan, M., Hangan, H., Wurman, J., Kosiba, K., 2017. Doppler radar-derived wind field of five tornado events with application to engineering simulations. Engineering Structures 148, 509-521. https://doi.org/10.1016/j.engstruct.2017.06.068

Rott, N., 1958. On the viscous core of a line vortex. Zeitschrift für angewandte Mathematik und Physik ZAMP 9, 543-553. https://doi.org/10.1007/BF02424773

Sabareesh, G.R., Matsui, M., Tamura, Y., 2012. Dependence of surface pressures on a cubic building in tornado like flow on building location and ground roughness. Journal of Wind Engineering and Industrial Aerodynamics 103, 50-59. https://doi.org/10.1016/j.jweia.2012.02.011

Sullivan, R.D., 1959. A Two-Cell Vortex Solution of the Navier-Stokes Equations. Journal of the Aerospace Sciences 26, 767-768. https://doi.org/10.2514/8.8303

Tang, Z., Feng, C., Wu, L., Zuo, D., James, D.L., 2017. Characteristics of Tornado-Like Vortices Simulated in a Large-Scale Ward-Type Simulator. Boundary-Layer Meteorology, 1-24. https://doi.org /10.1007/s10546-017-0305-7

Trapp R.J., 2000. A Clarification of Vortex Breakdown and Tornadogenesis. Monthly Weather Review 128, 888-895. https://doi.org/10.1175/1520-0493(2000)128<0888:ACOVBA>2.0.CO;2

Vatistas, G.H., Kozel V. and Mih, W.C., 1991. A simpler model for concentrated vortices. Experiments in Fluids, 11, 73–76. https://doi.org/10.1007/BF00198434

Vyas, A. B., Majdalani, J., and Chiaverini, M. J., 2003. The Bidirectional Vortex. Part 1: An Exact Inviscid Solution. AIAA 2003-5052. https://doi.org/10.2514/6.2003-5052

Ward, N.B., 1972. The Exploration of Certain Features of Tornado Dynamics Using a Laboratory Model. Journal of the Atmospheric Sciences 29, 1194-1204. https://doi.org/10.1175/1520-0469(1972)029<1194:TEOCFO>2.0.CO;2

Winn, W.P., Hunyady, S.J., Aulich, G.D., 1999. Pressure at the ground in a large tornado. Journal of Geophysical Research: Atmospheres 104, 22067-22082. https://doi.org/10.1029/1999JD900387

Wood, V.T., Brown, R.A., 2011. Simulated Tornadic Vortex Signatures of Tornado-Like Vortices Having One- and Two-Celled Structures. Journal of Applied Meteorology and Climatology 50, 2338-2342. https://doi.org/10.1175/JAMC-D-11-0118.1

Wood, V.T., White, L.W., 2011. A New Parametric Model of Vortex Tangential-Wind Profiles: Development, Testing, and Verification. Journal of the Atmospheric Sciences 68, 990-1006. https://doi.org/10.1175/2011JAS3588.1

Wurman, J., Gill, S., 2000. Finescale Radar Observations of the Dimmitt, Texas (2 June 1995), Tornado. Monthly Weather Review 128, 2135-2164. https://doi.org/10.1175/1520-0493(2000)128<2135:FROOTD>2.0.CO;2

Wurman, J., Kosiba, K., Robinson, P., 2013. In Situ, Doppler Radar, and Video Observations of the Interior Structure of a Tornado and the Wind–Damage Relationship. Bulletin of the American Meteorological Society 94, 835-846. https://doi.org/10.1175/BAMS-D-12-00114.1

Xu, Z and Hangan, H., 2009. An Inviscid Solution for Modeling of Tornadolike Vortices. Journal of Applied Mechanics 76, 031011-031011-031015. https://doi.org/10.1115/1.3063632